UNIVERSITY OF CALIFORNIA
SANTA CRUZ

DECODING ASTROVIRUS IMMUNITY: MAPPING THE ASTROVIRUS NEUTRALIZING EPITOPE LANDSCAPE AND PRELIMINARY VACCINE STUDIES

A dissertation submitted in partial satisfaction
of the requirements for the degree of

DOCTOR OF PHILOSOPHY

in

MOLECULAR CELL DEVELOPMENTAL BIOLOGY

by

Sarah Lanning

September 2024

The Dissertation of Sarah Lanning is approved:

_____
Professor Rebecca DuBois, thesis advisor

_____
Professor Seth Rubin

_____
Professor Valerie Cortez

_____

Peter F. Biehl
Vice Provost and Dean of Graduate Studies

TABLE OF CONTENTS:

LIST OF FIGURES:

Chapter 1:

Chapter 2:

Appendix 1:

LIST OF TABLES:

Chapter 1:

Chapter 2:

ABSTRACT:

Decoding Astrovirus Immunity: Mapping The Astrovirus Neutralizing Epitope Landscape and Preliminary Vaccine Studies

Sarah Lanning

Diarrheal diseases remain a leading cause of death for young children worldwide. However, the reduction of total child deaths from viral sources of diarrhea may be possible through preventative vaccination. Human astroviruses (HAstVs) are a significant cause of viral diarrhea, with young children and immunocompromised populations most at risk. Some evidence indicates that antibodies induced by childhood infection leads to protection in adulthood, suggesting that vaccination against human astrovirus may be possible, but no vaccine or approved therapeutics currently exist. To develop an effective vaccine, it is important to understand how antibodies target critical regions of the virus. However, few studies have explored what regions of the HAstV capsid are responsible for inducing neutralizing antibodies or how these antibodies neutralize HAstV infection.

In this thesis research, I have investigated the vulnerable antigenic regions on the HAstV capsid spike by structurally defining the epitopes of three neutralizing monoclonal antibodies, 3B4, 3H4, and 4B6 using X-Ray crystallography or cryogenic electron microscopy. I have discovered three new neutralizing antibody epitopes, with the epitope of antibody 3H4 being an entirely novel and highly conserved antigenic

location near the base of the spike. Additionally, all three of these antibodies block virus attachment to cells, and I show using biolayer interferometry that they either fully or partially block HAstV spike binding to the newly discovered HAstV receptor human neonatal Fc receptor (FcRn). Finally, I establish a proof-of-concept system to test a spike-based protein vaccine using the murine astrovirus (MuAstV) infection model in mice. I find that recombinant MuAstV spike folds into a native dimeric structure, and its use as a vaccine immunogen induces anti-spike IgG antibodies in mice, paving the way for future MuAstV challenge and vaccine protection studies. Taken together, my thesis research lays a foundation for HAstV vaccine design and monoclonal antibody therapies to prevent and treat HAstV infection and disease.

ACKNOWLEDGEMENTS:

The work presented in this dissertation was funded by the NIH NIAD training grant T32 GM133391 and NIH R01 AI144090.

The text of this dissertation includes reprints of the following previously published material: "Structure and Immunogenicity of the Murine Astrovirus Capsid Spike" (Lanning S, Pedicino N, Haley DJ, Hernandez S, Cortez V, DuBois RM. *J Gen Virol*. 2023; Vol 104, No.11) and "Structures of Two Human Astrovirus Capsid/Neutralizing Antibody Complexes Reveal Distinct Epitopes and Inhibition of Virus Attachment to Cells" (Ricemeyer L, Aguilar-Hernández N, López T, Espinosa R, Lanning S, Mukherjee S, Cuellar C, López S, Arias CF, DuBois RM. *J Virol.* 2022; Vol. 96, No.1). *The co-author, Rebecca M DuBois, listed in this publication directed and supervised the research which forms the basis for the dissertation. Other individual author contributions are listed in the respective chapter acknowledgements.*

~

This thesis is dedicated to everyone who believed in me

~

CHAPTER 1:

Discovery of Three Novel Neutralizing Antibody Epitopes on the Human Astrovirus Capsid Spike and Mechanistic Insights into Virus Neutralization

1.1 Acknowledgements

This chapter focuses on mapping the antigenic sites of the HAstV spike that induce neutralizing antibodies and characterizing the mechanism of antibody neutralization. This manuscript will soon be submitted to the Journal of Virology under the title "Discovery of Three Novel Neutralizing Antibody Epitopes on the Human Astrovirus Capsid Spike and Mechanistic Insights into Virus Neutralization" by Lanning S, Aguilar-Hernández N, Serrão VB, López T, O'Rourke S, Lentz A, Ricemeyer L, López S, Arias C, DuBois RM. My specific contributions to this work were the expressions of Fab 4B6 and scFv 4B6, the purification of Fab 4B6, 3H4, 3B4 and 4B6 scFv, forming and purifying the Fab 4B6 / HAstV2 spike and Fab 3B4 / Fab 3H4 / HAstV1 spike complexes, performing crystal trials of Fab 4B6 / HAstV2 spike including screen setup and optimizations, collecting diffraction data, processing the data and further refinements, as well as cryoEM data processing of the Fab 3B4 / Fab 3H4 / HAstV1 spike complex including modeling and further refinements, validating and submitting the final structures, performing the biolayer interferometry assays to

determine antibody affinities and also the biolayer interferometry assays of antibody competition with FcRn, writing the initial draft of the manuscript, figures, and further editing. Nayeli Aguilar-Hernández performed the assays involved in testing if 3B4, 3H4, and 3B4 block attachment or detach HAstV from cells. Vitor Hugo B Serrão prepared frozen grid samples for cryoEM, screened the samples on UCSC's Glacios microscope, and assisted with cryoEM data processing decisions and advised in final preparation of figures. Tomás López performed neutralization assays with scFv and mAb constructs, Sara O'Rourke expressed Fabs 3H4 and 3B4. Adam Lentz designed the FcRn construct, and expressed and purified the FcRn protein used in the biolayer interferometry assay. Lena Ricemeyer cloned Fab and scFv constructs of 4B6, 3H4, and 3B4 and expressed and purified HAstV1 and HAstV2 spike. Susana López, Carlos F. Arias, Rebecca M. DuBois conceptualized project ideas, supplied funding, supervised the work and edited the manuscript.

1.2 Abstract:

Human astroviruses (HAstVs) are a leading cause of viral childhood diarrhea that infect nearly every individual during their lifetime. Although human astroviruses are highly prevalent, no approved vaccine currently exists. Antibody responses appear to play an important role in protection from HAstV infection, however knowledge about the neutralizing epitope landscape is lacking, as only 3 neutralizing antibody epitopes have previously been determined. Here, we structurally define the epitopes of 3

uncharacterized HAstV-neutralizing monoclonal antibodies: antibody 4B6 with X-ray crystallography to 2.67 Å, and antibodies 3H4 and 3B4 simultaneously with cryogenic electron microscopy to 3.33 Å. We assess the epitope location relative to conserved regions on the capsid spike and find that while antibodies 4B6 and 3B4 target the upper variable loop regions of the HAstV spike protein, antibody 3H4 targets a novel region near the base of the spike that is more conserved. Additionally, we found that all 3 antibodies bind with high affinity and compete with receptor FcRn binding to the capsid spike. These studies inform which regions of the HAstV capsid are targetable by monoclonal antibody therapies and aid in rational vaccine design.

1.3 Introduction:

Human astroviruses (HAstVs) are a significant cause of childhood viral diarrhea worldwide, with over 35% children having had a HAstV infection by age 2.[1] These small nonenveloped RNA viruses are typically spread by fecal-oral or salivary routes.[2,3] While HAstV infections are typically self-limiting in immunocompetent people, they can persist as a chronic infection in immunocompromised individuals.[4,5,6] Young children and immunocompromised individuals are the populations most at risk for HAstV disease, particularly in lower-income or tropical countries where higher burdens of diarrheal disease and additional comorbidities may exist.[7,8] The classical HAstV clade includes eight serotypes (HAstV1-8), with serotype 1[9,10,11] being the most prevalent worldwide. Divergent VA and MLB clades,

which may have arisen from animal astroviruses, have been found to cause fatal encephalitis in immunocompromised individuals.[12] Encephalitic symptoms can also be caused by some animal astroviruses, such as mink and bovine astroviruses.[13,14] Despite HAstV's prevalence and global health impacts, there are currently no vaccines or HAstV-specific therapeutics available.

Some evidence suggests the presence of lasting HAstV immunity induced by prior infection.[1] Seroprevalence to HAstV in adults is very high (>90%)[15,16] and HAstV disease is rarer in adults than in children.[17] Additional studies have supported that the presence of anti-HAstV antibodies may help to protect from severe HAstV disease,[3] and one case study showed improvement of a patient with chronic HAstV disease after immunoglobulin therapy. Subsequently, it may be beneficial to develop a vaccine strategy which induces similar protective antibody responses as what is seen in natural infection. However, the mechanism of how antibodies neutralize HAstV is not well understood, in part due to a lack of knowledge surrounding how antibodies interact with the viral capsid, and which parts of the exposed viral capsid are critical for its function.

The HAstV virion consists of a small proteinaceous icosahedral capsid roughly ~40 nm in diameter, which shelters a ~7 kb single-stranded positive sense polyadenylated RNA genome.[18] The immature capsid is made up of 180 units of capsid protein originating from open reading frame 2 (ORF2), and displays a T=3 symmetry. The capsid protein is initially expressed as a 90 kD protein (VP90), which undergoes an intracellular caspase cleavage that is important for viral release from the

cell, resulting in a ~70 kD (VP70) protein after the loss of its C-terminal acidic domain.[19,20] In this state, the virus remains immature and must undergo further extracellular protease cleavage(s) to reach its mature infectious form.[21] The exact extracellular protease used *in vivo* for this cleavage event is unknown, but *in vitro* cleavage with trypsin results in a 10^5 fold increase in infectivity. This extracellular protease cleavage event cleaves VP70 into the core domain (VP34), and spike domain (VP25/VP27), and additionally removes 60 of the initial 90 dimeric spikes along 5-fold symmetry axes, resulting in 30 dimeric spikes (VP27) remaining on the mature capsid along the 2-fold symmetry axes.[22,23] The spike domain is known to be important for attachment and entry of the virus, and antibodies that target the spike domain have been found to neutralize HAstV in cell culture, whereas antibodies that target the core domain are not found to neutralize HAstV.[24,25] Recently, two preprint articles reported the identification of the neonatal Fc receptor (FcRn) as an important host receptor for human astrovirus entry, and FcRn was found to bind the HAstV capsid spike.[26,27] However, information about which regions of the spike are important for this interaction and how antibodies may interfere with this function remains mostly unexplored. Only three HAstV-neutralizing antibody epitopes have been structurally defined, revealing two neutralizing antigenic sites on the HAstV spike, since two of the neutralizing antibodies (3E8, PL-2) have overlapping epitopes.[28,29] Both neutralizing epitope regions were located around a conserved putative receptor binding site on the surface of the HAstV spike, known as the "P-site,"[30] and these antibodies were additionally shown to block spike attachment to

cells.[28] Whether these antibodies prevent FcRn binding or some other host factor interaction remains unknown. Furthermore, whether additional neutralizing antigenic sites exist on the HAstV spike remains unknown. Here, we structurally define three novel neutralizing antibody epitopes, assess their epitope location relative to conserved regions of the HAstV spike, and provide evidence supporting their mechanism of HAstV neutralization.

1.4 Results

1.4.1 HAstV-neutralizing antibodies 3B4, 3H4, and 4B6 bind with high affinity to the HAstV spike

We previously generated a panel of IgG1 monoclonal antibodies (mAbs), three of which were found to neutralize either HAstV1 (mAbs 3B4 and 3H4) or HAstV2 (mAb 4B6) in Caco-2 cells, the gold standard cell line used for HAstV propagation and infectivity studies. Here, we generated recombinant antigen-binding fragments (Fabs) of these HAstV-neutralizing antibodies to remove the avidity effects of a full bivalent mAb given the homodimeric nature of their target, the HAstV capsid spike domain. To determine binding affinities, biosensors loaded with HAstV spike were dipped into serial dilutions of Fabs. All three Fabs bind the corresponding HAstV spike with high affinities, with dissociation constants (K_D) in the mid-low nanomolar range (Table 1.1, Fig 1.1). These results indicate that vaccination with recombinant HAstV spikes are able to induce high affinity HAstV-neutralizing antibodies in mice.

Table 1.1: Antibodies 3B4, 3H4 and 4B6 bind HAstV spike with high affinity

Antibody to spike	Average $K_D \pm \sigma$ (nM)	χ^2	R^2
Fab 3H4 - spike 1	0.490 ± 0.002 nM	<0.2339	>0.9991
Fab 3B4 - spike 1	11.8 ± 0.5 nM	<0.7474	>0.9909
Fab 4B6 - spike 2	161 nM ± 2 nM	<0.0675	>0.9943

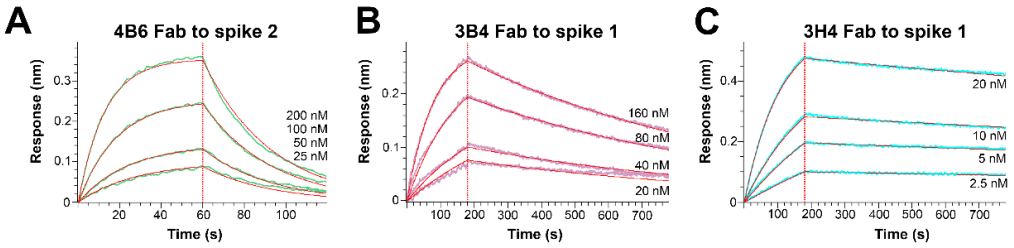

Figure 1.1: Antibodies 3B4, 3H4, and 4B6 bind HAstV spike with high affinity

(A) Biolayer interferometry (BLI) traces of a representative Fab 4B6 dilution series with global curve fits using a 1:1 model. **(B)** Biolayer interferometry (BLI) traces of a representative Fab 3B4 dilution series with global curve fits using a 1:1 model. **(C)** Biolayer interferometry (BLI) traces of a representative Fab 3H4 dilution series with global curve fits using a 1:1 model.

1.4.2 HAstV-neutralizing antibodies 3B4, 3H4, and 4B6 block attachment of HAstV to Caco-2 cells.

Since all 3 antibodies bind the HAstV spike with high affinity and the spike is believed to be responsible for attachment and entry, we tested whether mAbs 3B4, 3H4, or 4B6 could block attachment of HAstV to Caco-2 cells.. Caco-2 monolayers were incubated with HAstV-antibody complexes, or HAstV alone. Unbound virus was washed away and the bound virus was quantified using RT-qPCR. We found that

all three antibodies were able to block virus attachment to cells in a dose-dependent manner compared to a negative control antibody (Fig. 1.2).

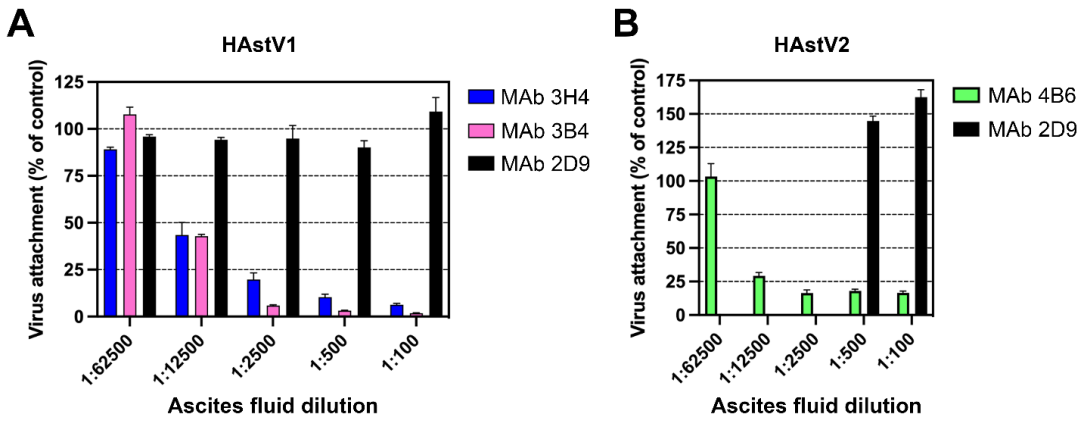

Figure 1.2: Monoclonal antibodies to HAstV1 and HAstV2 block attachment of the virus to Caco-2 cells

Ascitic fluid of **(A)** MAbs 3B4 or 3H4 to HAstV1, or **(B)** MAb 4B6 to HAstV2 block attachment when pre-incubated with the corresponding virus before cell adsorption. MAb 2D9 which is serotype specific to HAstV8 was used as a negative control. Experiments were performed on ice to prevent virus endocytosis. The assay was performed in biological quintuplicates and carried out in duplicate. The data are expressed as percentages of the virus attached in the absence of antibodies and represent the mean ± SEM.

We also tested the ability of the three antibodies' ability to displace virus that is bound to cells. HAstV was incubated on Caco-2 cell monolayers for 1 hr on ice, then virus-bound cells were incubated with serial dilutions of the three antibodies for an additional hour and then washed. Remaining virus was quantified by RT-qPCR. Interestingly, only 4B6 was able to detach already bound virus (Fig. 1.3). This detachment does not appear to be a function of a high affinity displacement, as 4B6 had the lowest affinity of the three antibodies (Table 1.1). This indicates that other factors, such as the binding location, may play a role in an antibody's ability to detach

virus. It could also be possible that the serotype of the virus is related to its ability to detach virus since 3H4 and 3B4, which were not able to detach the virus, both neutralize HAstV1, whereas 4B6 neutralizes HAstV2.

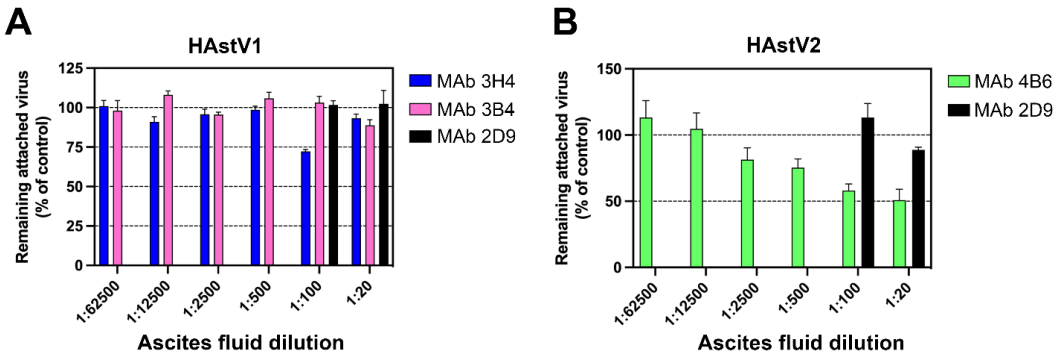

Figure 1.3: Monoclonal antibodies to HAstV1 and HAstV2 block attachment of the virus to Caco-2 cells

(A) HAstV1 or **(B)** HAstV2 were attached to cells on ice to prevent virus endocytosis. Subsequently, either ascitic fluid of **(A)** MAb 3B4 or 3H4, or **(B)** MAb 4B6 was added to cells and incubated for 1 h on ice. The remaining attached virus was determined by RT-qPCR. MAb 2D9 which neutralizes HAstV1 was added as a negative control. The assay was performed in biological sextuplicates and carried out in duplicate. The data are expressed as percentages of the virus that remained attached in the absence of antibodies and represent the mean ± SEM.

1.4.3 HAstV-neutralizing antibodies 3B4, 3H4, and 4B6 compete with FcRn binding to HAstV spike

With the recent discovery of neonatal Fc receptor (FcRn) as a critical receptor for HAstV infection, we investigated whether the HAstV-neutralizing antibodies 3B4, 3H4, and 4B6 could compete with FcRn's ability to bind to the HAstV spike. Either HAstV1 or HAstV2 spikes were loaded onto biosensors and then dipped into saturating levels of Fab 3H4, 3B4, or 4B6. The biosensors were then dipped into FcRn and these binding shifts were compared to the binding shifts of FcRn to spike-

loaded biosensors in the absence of Fab. From this assay, we determined that Fabs 3H4 and 4B6 fully block FcRn binding (Table 1.2), suggesting that these Fabs either directly or sterically block FcRn's ability to bind the spike protein, which may explain, at least partially, their mechanism of neutralizing HAstV. Fab 3B4 does not appear to fully block FcRn binding, but reduces FcRn binding to 40% of the control. Given that 3B4 is still efficient at neutralizing HAstV1, Fab 3B4 may have an alternative mechanism of neutralizing HAstV, such as blocking the interaction of another putative receptor, or the full-length mAb may be necessary for full steric hinderance of the FcRn interaction with HAstV1 spike. These data reveal that a mechanism of antibody neutralization may be blocking the FcRn interaction with the HAstV spike.

Table 1.2: Antibodies 3H4, 3B4, and 4B6 compete with FcRn receptor to spike

	Fab 3B4	Fab 3H4	Fab 4B6	FcRn
Fab 3B4	0			0.3944
Fab 3H4		0		0.03505
Fab 4B6			0	0.0630
no Fab				1.0000

0 Complete blocking
1 No blocking

1.4.4 HAstV2-neutralizing antibody binds to a distinct epitope on the upper loops of HAstV2 spike

Currently the epitopes for only three HAstV-neutralizing monoclonal antibodies have been structurally defined, which revealed two immunogenic sites on the spike. Subsequently, we sought to characterize three additional neutralizing antibodies, 3B4, 3H4, and 4B6, to determine if other immunogenic sites on the HAstV spike exist.

Previous escape mutation studies identified two adjacent amino acid changes in the HAstV2 spike, D564E and N565D, which allowed HAstV2 to overcome the neutralizing activity of antibody 4B6.[25] However, epitope of mAb 4B6 has not been structurally defined. To visualize where neutralizing antibody 4B6 binds to the HAstV spike, we solved the crystal structure of the recombinant single-chain variable fragment (scFv) 4B6 in complex with the HAstV2 spike to 2.67 Å resolution (Fig. 1.4,A). This structure revealed that 4B6 binds to a novel 694 $Å^2$ quaternary epitope at the top of the spike. Each chain of 4B6 interacts predominantly with the long loop 3 from the opposing protomer, with some residues in the CDR-H3 loop of the heavy chain interacting with both protomers (Fig. 1.4B,C,D). All 3 CDR's in 4B6 heavy chain interact with the spike, but in the light chain, only CDR-L1 and CDR-L3 interact. Antibody 4B6 forms a network of 8 hydrogen bonds with spike residues 563-567 at the very tip of loop 3, which interact with both light chain CDR L3 residues Y226-Y231 and heavy chain CDR H3 residues D102 and T99 (Fig. 1.4C). This hydrogen bond network consists of a mix of side-chain and backbone interactions for both the antibody and spike. This data correlates with the two residues D564 and N565 on loop 3 that were previously identified as locations for escape mutations to antibody 4B6—the mutation of these two residues would disrupt at least 2 hydrogen bond interactions, which may explain how these escape mutations disrupt 4B6 neutralization of HAstV (Fig. 1.4C). The HAstV spike loop 3, which 4B6 primarily targets, is highly variable across strains of HAstV, which may indicate that this

location is particularly immunogenic and frequently targeted by antibodies, creating selective pressure for the virus to mutate this region.

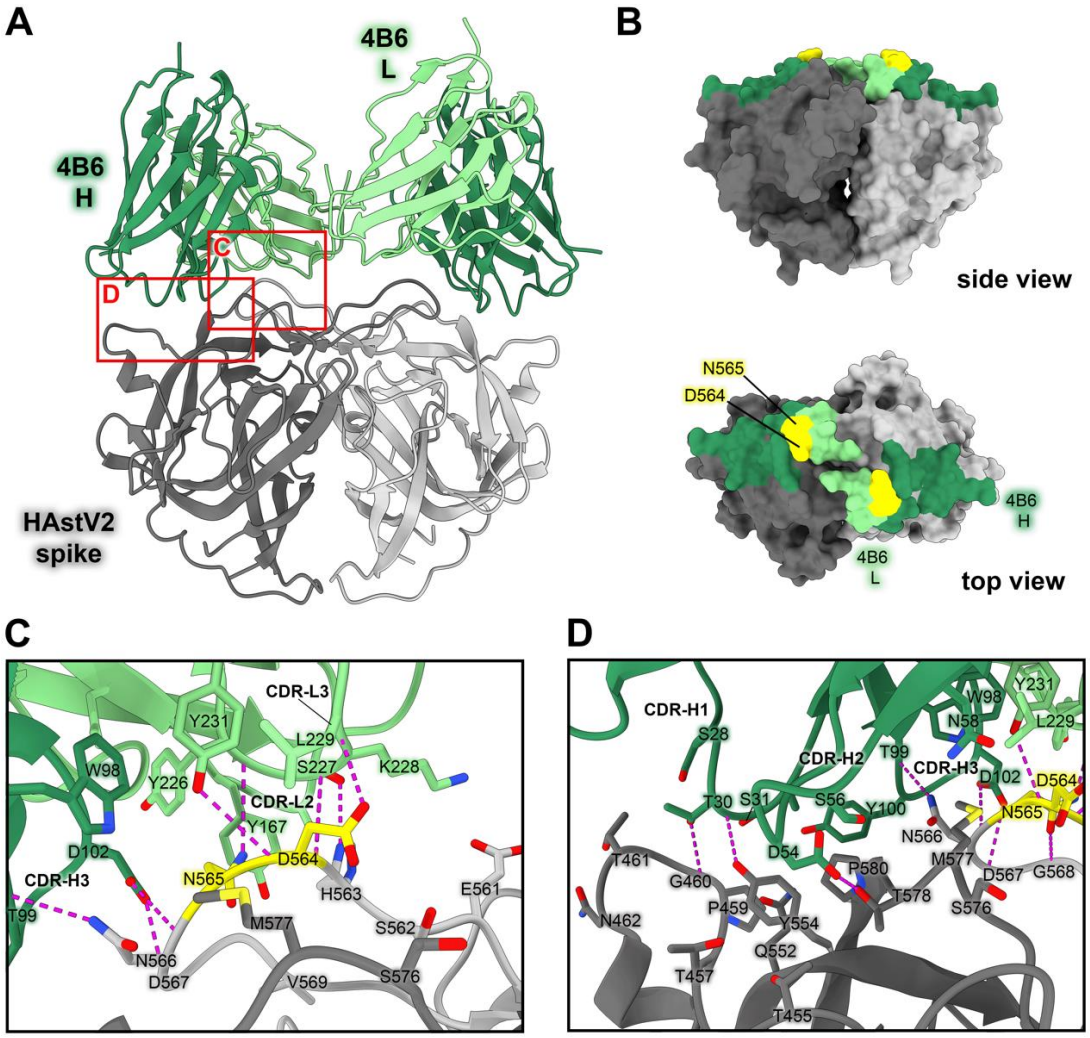

Figure 1.4: Neutralizing antibody 4B6 binds to a unique epitope on the top of the HAstV2 spike

(A) Crystal structure of scFv 4B6 bound to the HAstV2 spike homodimer solved to 2.67 Å resolution and displayed as a ribbon model. The spike is colored grey and scFv 4B6 is colored green, with the heavy chain colored dark green and light chain colored light green. Red panels show the locations of the focused views shown in panels C and D. **(B)** Surface model of the HAstV2 spike with residues involved in the 4B6 epitope colored in dark green for a heavy chain interactions or light green for light chain interactions. The yellow residues indicate previously identified escape

mutation locations to antibody 4B6.[25] **(C)** Focused view on the light chain interaction, with 4B6 light chain colored light green. Side chains involved in hydrogen bonding are shown, with hydrogen bonds colored magenta. 4B6 light chain predominantly interacts with spike loop 3. **(D)** Focused view on the heavy chain interaction, with 4B6 heavy chain colored dark green. 4B6 heavy chain predominantly interacts with beta sheets 8 and 11, and the tip of loop 3 on the HAstV spike.

Table 1.3: Crystallographic statistics for scFv 4B6 - HAstV2 spike complex

PDB: 9CN2	
Data collection:	
Space group	P 41 3 2
Cell dimensions	
a, b, c (Å)	160.348, 160.348, 160.348
α, β, γ (°)	90, 90, 90
Resolution (Å)	160.64-2.67 (2.72-2.67)
Rmerge	0.191 (3.291)
I/σl	23.4 (1.0)
Completeness	100% (100%)
Multiplicity	74.5 (55.5)
$CC_{1/2}$	0.999 (0.755)
Refinement:	
Wavelength:	1.0332
Resolution (Å)	40.09-2.67 (2.76-2.67)
No. reflections for refinement	20582
No. reflections for R_{free}	1997 (197)
R_{work}/R_{free}	0.2234/0.2647
No. atoms	3496
Protein	3493
Ligand/ion	0
Water	3
B-factors (Å2):	72.28
Protein	72.29
Ligand/ion	N/A
Water	60.18

Protein residues:	444
RMSD:	
Bond lengths	0.009
Bond angles	1.11
Ramachandran statistics	
Favored (%)	96.58
Allowed (%)	3.42
Outliers (%)	0

1.4.5 HAstV1-neutralizing antibody 3H4 binds to a novel epitope near the base of the spike, and HAstV1-neutralizing antibody 3B4 binds the top dimer interface in a unique asymmetric way

Previous escape mutation studies revealed a single point mutation K504E (for 3H4) or S560P (for 3B4) in the HAstV1 spike that allowed the virus to escape the neutralizing effects of antibody 3H4 or 3B4. To define the full epitopes of antibodies 3H4 and 3B4, we solved the structure of both Fabs 3H4 and 3B4 in complex with the HAstV1 spike to 3.33 Å resolution using cryoEM (Fig. 1.5A,B, Fig 1.6A,B). This structure reveals two novel epitopes, with a single Fab 3B4 bound to the top of the spike dimer interface, and two Fab 3H4 bound to the bottom sides of the spike dimer (Fig. 1.5A,B). Antibody 3B4 spans a 1039 $Å^2$ quaternary epitope across the top dimer interface, with more of the epitope located on one protomer than the other (Fig. 1.5A,E). Based on the structure, as well as the retention volume of the complex in solution on a size-exclusion chromatography column, only one 3B4 antibody can bind the spike homodimer at a time, which represents the first antibody of its kind to be discovered for HAstV, as all other previously characterized antibodies can bind

symmetrically with one antibody binding site per protomer. Antibody 3B4 targets the majority of loop 3 on one monomer closer to the base of the loop, and the side of loop 3 on the other monomer. Although 3B4 has sizeable overlap with the 4B6 epitope, it interacts with unique residues focused more on the center of the dimer interface, while 4B6 is targeted more outward towards the tips of loop 3. All six of 3B4 CDR loops interact with the spike, forming a hydrogen bond network primarily between spike residues G573-T577, and 3B4 residues S30-N32 on CDR-L1 (Fig. 1.5C). Q53 and S50 from CDR-L2 also contribute several hydrogen bonds, with Q53 making two hydrogen bonds with T613 and N614. On the heavy chain, the majority of the hydrogen bonds are contributed by CDR-H1 residues T28 and T30, which target T562 and S560 on the spike. Although a single point mutation of S560P in the spike sequence confers resistance to antibody 3B4 neutralization, this mutation actually changes two distinct sites of interaction with the heavy chain of 3B4, given the close locations of each S560 to each other on the dimer interface (Fig. 1.5C,E). This could suggest that single point mutations offer higher resistance to dimer interface antibodies in comparison to antibodies that bind both protomers.

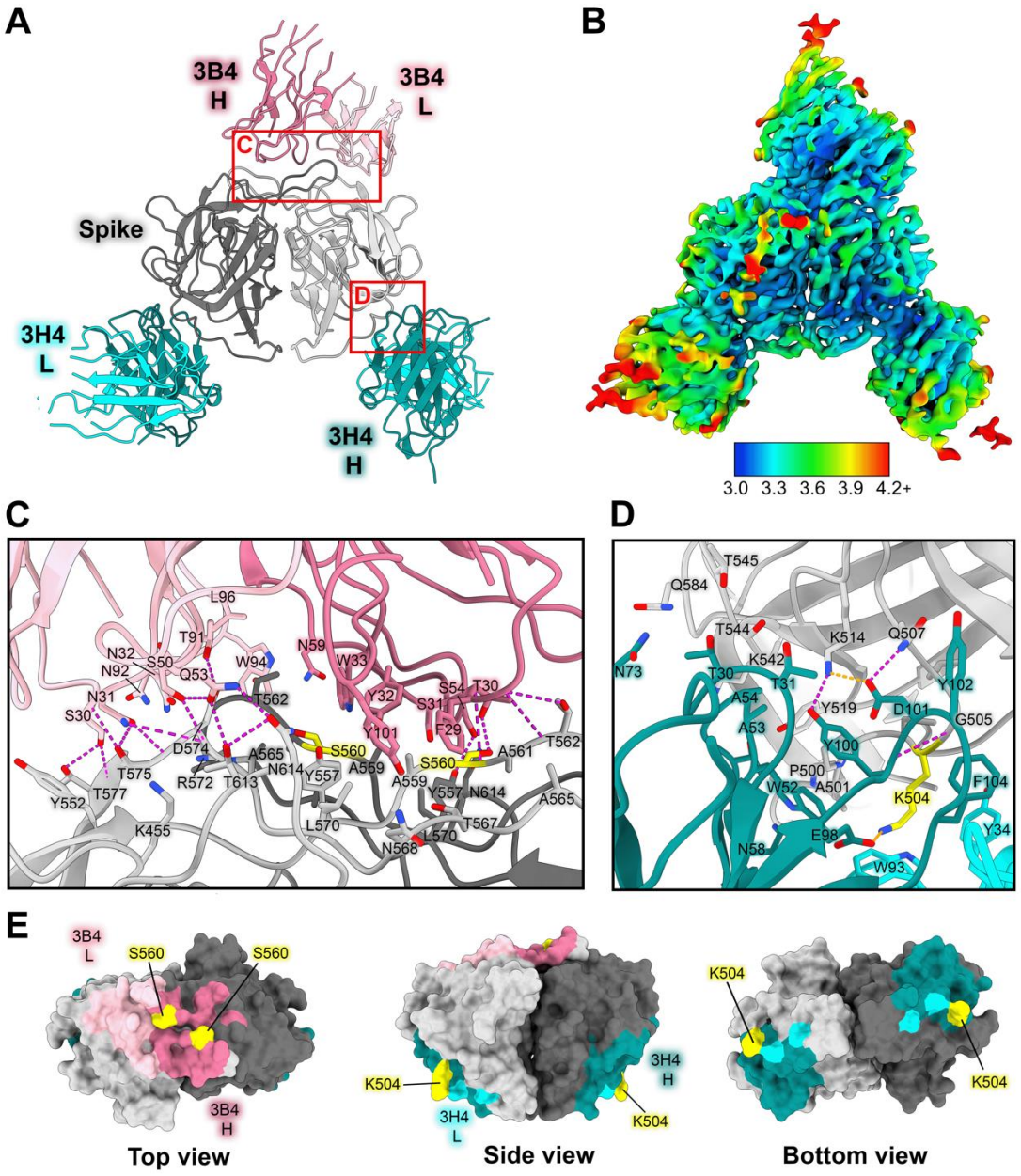

Figure 1.5: Neutralizing antibody 3H4 binds to a unique epitope at the base of the spike, and neutralizing antibody 3B4 has a unique top epitope in which a single antibody binds the spike dimer interface

(A) CryoEM structure solved to GSFSC 3.33 Å of neutralizing Fab 3H4 and Fab 3B4 bound simultaneously to the HAstV1 spike, displayed as a ribbon model with 3H4 colored cyan and 3B4 colored pink. The heavy and light chains are colored in dark and light shades, respectively. Red panels show the locations of the focused views shown in panel C and D. **(B)** Local resolution of the cryoEM structure of HAstV1 spike bound to 3H4 Fab and 3B4 Fab, with EM volume threshold set to 0.043 in ChimeraX. **(C)** Focused view of the 3B4 epitope, with the light chain colored light pink, and the heavy chain colored dark pink, with hydrogen bond interactions colored magenta. Serine 560, which was previously identified as a residue that overcomes the neutralization activity of 3B4 when mutated to proline, is highlighted in yellow. **(D)** Focused view of the 3H4 epitope, with the light chain colored light cyan, and the heavy chain colored dark teal. Hydrogen bond interactions are colored magenta and salt bridges are colored in orange. Lysine 504, which was previously identified as a residue that overcomes the neutralization activity of 3H4 when mutated to glutamic acid, is highlighted in yellow. **(E)** Surface view of the HAstV1 spike with antibody interacting residues colored according to antibody chain. Residues interacting with both chains are colored according to the predominant interaction. Residues which confer resistance to the respective antibody when mutated are colored in yellow.

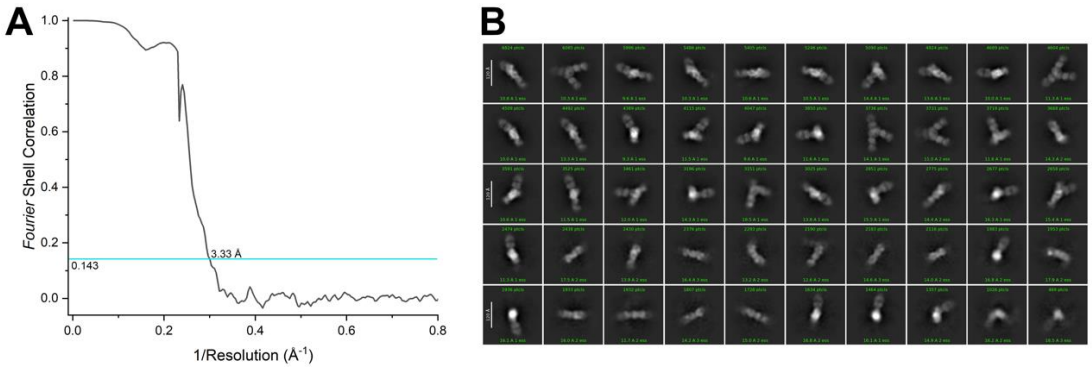

Figure 1.6: Fab 3B4 and 3H4 bound to HAstV1 spike single-particle cryoEM reconstruction

(A) $FSC_{0.143}$ with an overall resolution of 3.33 Å. **(B)** Representative 2D classes.

Table 1.4: Statistics for cryoEM structure of Fab 3B4 / Fab 3H4 / HAstV1spike complex

Data collection information	***PNCC #160258 – Krios-3***
Nominal magnification	105,000x
Voltage (kV)	300
Electron dose ($e^-/Å^2$)	32.26
Physical pixel size (super-res) (Å)	0.415
Movies amount	7,235
Defocus average and range (μm)	-1.5 (-2.5 to -0.5)
Frames	60
Single-particle reconstruction information	**EMDB 45427**
Initial particles picked	4,132,753
Particles in the final map	163,237
Initial model used	PDB 5EWO, ab-initio
Symmetry imposed	C1
Map overall resolution - $FSC_{0.143}$ (Å)	3.33
Map resolution range (Å)	3.0-4.2
Map sharpening	
B-factor ($Å^2$)	-112
Built model information	**PDB 9CBN**
Chains	11
Atoms (non-H)	10967
Protein residues	1,040
Water	0
Ligands:	
BMA:	2
NAG:	5
Bonds (RMSD)	
Length (Å, # > 4σ)	0.020 (2)
Angles (°,# > 4σ)	1.536 (91)
Mean B-factor ($Å^2$)	
Protein	0.78/102.01/40.47
Nucleotide	N/A
Ligand	30.00/56.36/50.22
Water	N/A
MolProbity score	2.72
Clashscore	31.17
Ramachandran plot	

Favored (%)	92.24
Allowed (%)	7.76
Outliers (%)	0
Rama-Z (Ramachandran plot Z-score, RMSD)	
Whole (N = 3625)	-2.05 (0.26)
Helix (N = 1443)	-5.16 (0.42)
Sheet (N = 472)	-1.26 (0.26)
Loop (N = 1710)	-1.36 (0.25)
Rotamer outliers (%)	2.22
Cβ outliers (%)	1.77
Peptide plane (%)	
Cis proline/general	7.3/0.0
Twisted proline/general	0.0/0.0
CaBLAM outliers (%)	3.49
Occupancy	
Mean	1
occ = 1 (%)	99.26
0 < occ < 1 (%)	0.74
occ > 1 (%)	0
Model vs. Data	
Mean CC for ligands	0.64
CC (peaks)	0.64
CC (volume)	0.75
CC (box)	0.7
CC (mask)	0.78

Despite both 4B6 and 3B4 targeting loop 3, 3B4 targets residues that are more conserved. Fab 3H4 binds to a novel 676 $Å^2$ epitope near the base of the spike which is distinct from any other known HAstV-neutralizing antibody epitope, as all previously solved spike-antibody structures target the top or upper sides of the spike dimer (Fig. 1.7A,B). The 3H4 epitope interaction is facilitated almost entirely by the heavy chain alone, with only W93 from CDR L1 and Y34 CDR L3 from the light chain making any contact with the spike (Fig. 1.5D,E). Antibody 3H4 mostly targets

the upper portion of the spike loop 2 with all 3 heavy chain CDR loops. Two salt bridges formed between K514 on spike and D101 on CDR-H3, and K504 with E98 on CDR-H3 (Fig. 1.5D). These lysines also form hydrogen bonds and cation-pi interactions with 3H4. Notably, the salt bridge interaction by K504 appears critical to the ability of 3H4 to bind to spike as the mutation of K504 to a negatively-charged glutamic acid disrupts 3H4 neutralization of HAstV1. Antibody 3H4 also targets a region of much higher conservation than that of the other antibodies, with over 70% of the interacting spike residues being semi-conserved or higher amongst the 8 HAstV serotypes. Despite the majority of residues being conserved, K504, which is critical to 3H4 neutralization, is highly variable among serotypes, which likely accounts for the 3H4 serotype specificity.

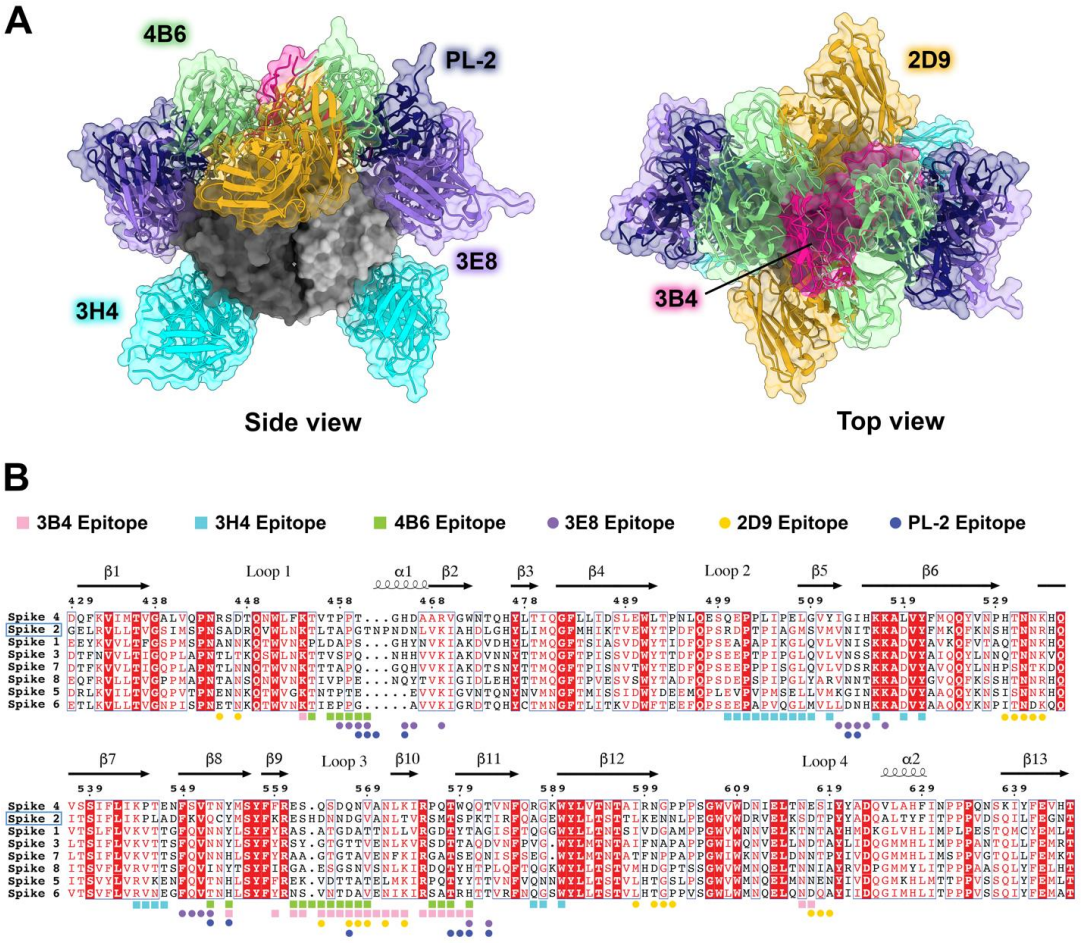

Figure 1.7: Comparison of all known HAstV-neutralizing antibody epitopes, showing that most target the upper variable region of HAstV spike

2.1.1 **(A)** Alignment of all existing HAstV neutralizing antibody structures 4B6, 3B4, 3H4, 3E8, 2D9, and PL-2, mapped onto HAstV1 spike. **(B)** Spike protein sequences of the eight classical HAstV serotypes aligned using EMBL-MUSCLE, with residues colored according to conservation. The following sequences were used for the alignment: HAstV1, GenBank #AAC34717.1; HAstV2, GenBank # KY964327.1; HAstV3, Uniprot #Q9WFZ0.1; HAstV4, Uniprot #Q3ZN05.1; HAstV5, Uniprot #Q4TWH7.1; HAstV6, Uniprot #Q67815.1; HAstV7, Uniprot #Q96818.2; HAstV8, Uniprot #Q9IFX1.2. Residues highlighted in red are strictly conserved, residues with red text are semi-conserved, and residues in black text have little to no conservation. Spike residues interacting with the antibodies characterized in this paper, 3H4, 3B4, and 4B6, are indicted with colored squares, and epitope residues for antibodies which were previously characterized, 2D9, 3E8, and PL-2, are indicated as colored circles.

1.4.6 scFv 3H4, 3B4 and 4B6 neutralize HAstV

Antibody 3H4 reveals a particularly interesting epitope location, as the full-length antibody would likely clash with the icosahedral core of the HAstV capsid, suggesting that this antibody may contort the spike dimer in some way. Since 3H4 binds so distantly from other structurally determined neutralizing antibody epitopes and yet is still shown to block FcRn receptor binding, we hypothesized that 3H4 may neutralize HAstV by steric hinderance with its constant regions and contortion of the spike, rather than the direct blocking of an important functional site on the spike. We tested whether scFv 3H4 3B4 and 4B6, which lack antibody constant domains, could still neutralize HAstV. HAstV1 was preincubated with serial dilutions of scFv 3H4, scFv 3B4, or mAb 3B4 as a control, or HAstV2 was preincubated with scFv 4B6, then incubated on Caco-2 cell monolayer, and viral infection was measured by an immunoperoxidase focus-forming assay. We found that both the scFv 3H4 and 3B4 are still able to neutralize HAstV1 and do so to a similar degree, but are not as effective at neutralization as full-length mAb (Fig. 1.8B), indicating that steric hinderance and/or avidity have a role in the ability of these antibodies to neutralize virus. scFv 4B6 was most effective at neutralizing virus of the scFvs (Fig 1.8B) despite having the lowest affinity, indicating that affinity may not always correlate with neutralization ability, and factors such as binding location may contribute to the ability to neutralize.

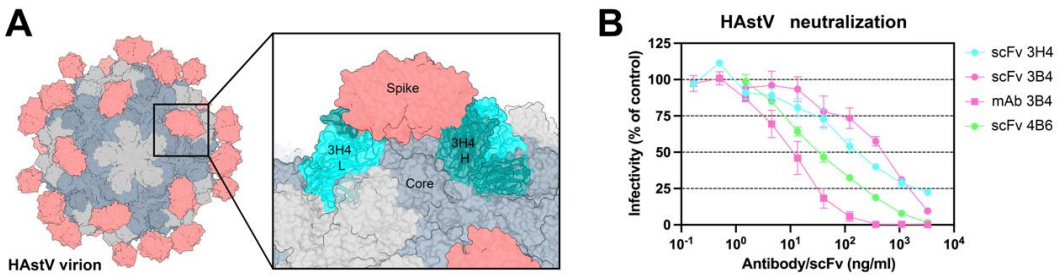

Figure 1.8: Steric hindrance from the antibody 3H4 constant domains may play a role it its ability to neutralize HAstV1

(A) Graphic depicting the full virion capsid constructed as described previously, with the core domains colored in grey and the spike domains colored in salmon. The panel shows a focused view of how Fab 3H4 would clash with the HAstV capsid core, using the solved structure of 3H4 variable domain and an aligned AlphaFold 3 constant domain. **(B)** Neutralization activity of scFv 3H4, scFv 3B4, and mAb 3B4 against HAstV1 and scFv 4B6 against HAstV2. HAstV was preincubated with the corresponding scFv or mAb at the indicated concentrations. The infectivity of the virus was determined as described in Materials and Methods. The infectivity assay was performed in biological triplicates and carried out in duplicate. The data are expressed as % infectivity of control and represent the mean ± SEM.

1.4.7 AlphaFold 3 prediction accuracy

As predictive protein structural software advances, we sought to assess how accurately the recent release of AlphaFold 3 (AF3) could predict antibody-antigen interactions.[31] We compared the crystal structure of scFv 4B6 and HAstV2 spike with that of its AlphaFold 3 prediction, and found that not only was the antibody placed correctly, but even the side chain interactions were highly accurate (Fig.1.9A,D). However, on a macroscopic scale, the dimer interfaces appear to be slightly misaligned, causing the other protomer alignment and subsequent interacting residues to be slightly misaligned (Fig.1.9E), though the local side chain orientations still appear to be highly accurate. AF3 was confident in its prediction, with pTM of 0.88

and ipTM of 0.86. The overall accuracy of the AF3 model is quite high, with a TM-score of 0.97 (TM value of 1=identical match) when the AF3 model is aligned to the crystal structure. This is a substantial improvement from the AlphaFold 2 (AF2) prediction, which did not place scFv 4B6 in the correct general placement, let alone correct side chain orientations. (Fig.1.9A) We additionally compared the AF3 model of Fab 3H4 and Fab 3B4 with our solved cryoEM structure. The AF3 model of Fab 3H4 bound to HAstV1 spike was highly accurate (Fig.1.9B), with TM-score of 0.99 when aligned to the cryoEM structure with Fab 3B4 removed. Despite the higher TM-score, AF3 reported slightly lower confidence scores, with ipTM=0.78, and pTM=0.81. The AF3 predicted model for 3H4 additionally showed dramatic improvement from the AlphaFold 2 (AF2) prediction, which did not place Fab 3H4 in the correct general placement. In the case of Fab 3B4, AF3 could not successfully find the correct general placement and consistently placed 3B4 Fab on the side of the spike dimer (Fig.1.9C), even when we tried alternative searches for one or two Fabs or scFvs. Because the overall interface alignment appears to be slightly off in these AF3 models, this may explain why AF3 could not predict the epitope of Fab 3B4 correctly, which targets the dimer interface. AF3 was less confident in its predicted model of one Fab 3B4 bound to HAstV1 spike, with ipTM=0.52 and pTM=0.61, but were still above the 0.5 threshold suggesting that the structure could be correct, despite being an incorrect placement. However, the decrease in these scores for 3B4 compared to 3H4 and 4B6 does suggest some ability to determine whether the predicted structure is correct. From these assessments, AlphaFold 3 appears to have a

dramatic increase in accuracy compared to previous versions which consistently failed to predict antibody interactions at all, even though some challenging antibodies which target interfaces may still be more difficult.

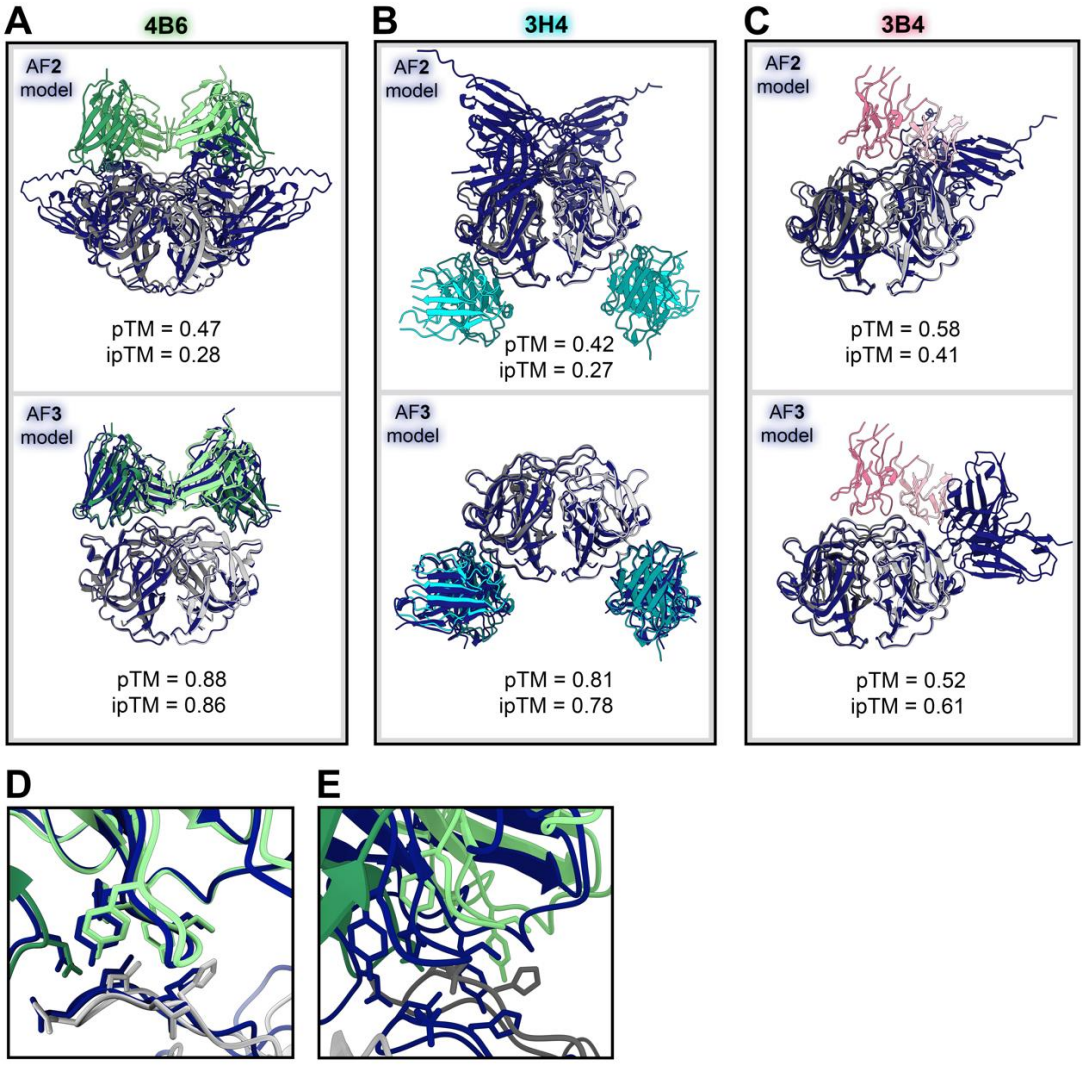

Figure 1.9: AlphaFold 3-predicted model of scFv 4B6 bound to HAstV2 spike and Fab 3H4 bound to HAstV1 spike is mostly accurate

(A) Crystal structure of antibody scFv 4B6 bound to HAstV2 spike (in green and grey) aligned in ChimeraX with the AlphaFold 2 predicted model (in navy blue, above) or AlphaFold 3 predicted model (in navy blue, below) **(B)** CryoEM structure of the variable domain of Fab 3H4 bound to HAstV1 spike (in cyan and grey) aligned in ChimeraX with the AlphaFold 2 predicted model (in navy blue, above) or

AlphaFold 3 predicted model (in navy blue, below). **(C)** CryoEM structure of the variable domain of Fab 3B4 bound to HAstV1 spike (in pink and grey) aligned in ChimeraX with the AlphaFold 2 predicted model (in navy blue, above) or AlphaFold 3 predicted model (in navy blue, below). **(D)** Focused view of the crystal structure light chain CDR-L3 loop interacting with the tip of HAstV2 spike loop 3 aligned with the AlphaFold 3 predicted model. **(E)** Focused view of the opposing spike protomer at the same location as in panel D.

1.5 Materials and Methods

1.5.1 Cells and viruses

Caco-2 cells, clone C2Bbe1 (ATCC), were propagated in high-glucose Dulbecco's modified Eagle's medium (DMEM-HG) (Sigma) supplemented with nonessential amino acids (Gibco) and 15% fetal bovine serum (FBS) (Cansera) in a 10% CO_2 atmosphere at 37°C. HAstV serotypes 1 and 2 have been described previously. All viral strains were activated with trypsin and grown as described before.

1.5.2 Expression and purification of recombinant HAstV1 and HAstV2 capsid spike proteins

Recombinant HAstV1 and HAstV2 spikes were produced as described previously. Briefly, cDNA corresponding to HAstV1 capsid protein residues 429 to 645 (GenBank: AAC34717.1) or HAstV2 Oxford strain capsid protein residues 429 to 644 (GenBank: KY964327.1) were cloned into pET52B with a C-terminal thrombin cleavage site and a 10-histidine purification tag sequence. Recombinant spikes were expressed in *Escherichia coli* BL21(DE3) and purified from soluble lysates by

HisTrap metal-affinity chromatography. Purified HAstV spikes were dialyzed into TBS (10 mM Tris pH 8.0 and 150 mM NaCl).

1.5.3 Expression and purification of recombinant monoclonal antibody Fabs 3B4, 3H4, and 4B6

The protein-coding sequence of antibodies 3H4, 3B4, and 4B6 heavy and light chains were determined as described previously. The protein-coding sequences of 3H4, 3B4, and 4B6 light chain and the 3H4, 3B4, and 4B6 heavy chain antigen binding fragment (Fab) were cloned into separate pCMV plasmids in frame with an N-terminal human IgG1 signal sequence. The Fab heavy chains were cloned in frame with a C-terminal thrombin-cleavable double StrepTagll affinity tag. A total of 120 μg of heavy chain plasmid and light chain plasmid combined were added to 8 x 10^7 CHO-S cells in an OC-400 cuvette (MaxCyte) and were electroporated. CHO-S cells were resuspended in CD-OptiCHO media (Gibco: #12681029) and fed CHO feed (CHO CD EfficientFeed A (Gibco: #A1023401) supplemented with 7 mM L-glutamine, 5.5% glucose, and 23.4 g/L yeastolate) every 24 hours. CHO-S cells were given a final concentration of 1 mM sodium butyrate and maintained at 32 °C, 8 % CO_2, 85% humidity, 135 rpm, 24 hours after electroporation for 8-10 days. CHO-S cells were centrifuged, and the resulting supernatants were given 1X protease inhibitor cocktail (Millipore 539137), BioLock (Iba Lifesciences 2-0205-050) to block free biotin in the media, and Strep Wash Buffer (50 mM Tris pH 7.4, 150 mM NaCl, 1mM EDTA), and were 0.22 μm filtered. Samples were loaded onto a regenerated StrepTrap HP 5 ml

column (Cytiva), washed with Strep Wash Buffer, and eluted with an increasing linear gradient of Strep Elution Buffer (Strep Wash Buffer + 2.5 mM desthiobiotin).

1.5.4 Expression and purification of recombinant monoclonal antibody scFv 3B4, 3H4, 4B6

A cDNA construct encoding the 4B6 variable heavy chain, a GGS$(GGGGS)_3$ linker, and the 4B6 light chain was cloned into the pCMV plasmid in frame with an N-terminal human IgG1 signal sequence and a C-terminal thrombin-cleavable double StrepTagll affinity tag. A total of 120 µg of this plasmid was added to 8 x 10^7 CHO-S cells and was electroporated. scFv 4B6 expression and purification was performed as described above for Fabs. Purified scFv was dialyzed into TBS. Synthetic genes for scFv 3H4 and 3B4 constructs were designed with the light and heavy chain variable domains connected by a GGS$(GGGGS)_3$ linker and flanking BgIII and NheI restriction sites. The gene was codon optimized for *Drosophila melanogaster* and ordered from Integrated DNA Technologies. The gene was cloned into a pMT_puro_BiP vector via restriction digest in frame with an N-terminal BiP secretion signal and a C-terminal thrombin cleavable double StrepII affinity tag in the vector. pMT-puro_BiP vectors containing scFv 3H4 and scFv 3B4 we Expression and purification was performed as described previously re used to make stably transfected Schneider 2 (S2) cells as described previously.

1.5.5 Expression and purification of recombinant neonatal Fc receptor (FcRn)

Codon optimized cDNA encoding the ectodomain of the FCGRT gene (UniProt: P55899, Met1-Ser297) or the β-2-Microglobulin gene (UniProt: P61769, Met1-Met119) were cloned separately into a derivative pCDNA3.1 vector. The FCGRT construct also contained a C-terminal thrombin-cleavable double StrepTagll affinity tag. A total of 40 µg of FCGRT plasmid and 80 µg of β-2-Microglobulin plasmid were added to 8 x 10^7 CHO-S cells and electroporated. CHO cell expression was performed as described above. The supernatant was loaded onto a StrepTrap XT affinity column (Cytiva), washed with Strep Wash Buffer, and eluted with Elution Buffer (Strep Wash containing 50mM biotin). Purified FcRn was dialyzed into TBS.

1.5.6 Binding assays of HAstV in the presence of neutralizing antibodies

Serial 1:5 dilutions of the ascitic fluids for 3B4, 3H4, or for 4B6, were pre-incubated with infectious, purified HAstV1 or HAstV2 particles, respectively (multiplicity of infection [MOI] = 30), for 1 h at room temperature. Caco-2 cell monolayers grown in 48-well plates were washed once with PBS, and then blocking solution (1% BSA in PBS) was added for 45 min at room temperature, followed by a 15 min incubation on ice. The cells were then washed once with ice-cold PBS and incubated with the virus-antibody complex for 1 h on ice. MAb 2D9, which neutralizes HAstV8, was used as a negative control. The unbound virus was washed three times with cold PBS, and the total RNA was extracted with TRIzol Reagent (Invitrogen) according to the manufacturer's instructions. Viral RNA or cellular 18S RNA was reverse transcribed using MMLV reverse transcriptase (Invitrogen). RT-qPCR was performed with the

premixed reagent Real Q Plus Master Mix Green (Amplicon), and the PCR was carried out in an ABI Prism 7500 Detection System (Applied Biosystems). The primers used to detect HAstV1 RNA were Fwd 5' - ATGAATTATTTTGATACTGAAGAAAATTACTTGGAA - 3' and Rev 5' - CTGAAGTACTTTGGTACCTATTTCTTAAGAAAG - 3'. For detection of HAstV2 RNA were Fwd 5' -ATGAATTATTTTGATACTGAAGAAAGTTATTTGGAA - 3' and Rev 5' - CTGAAGTACTGTGGTACCTATTTCTTAAGAAAG - 3'. For normalization, 18S ribosomal cellular RNA was amplified and quantified using forward primer 5'- CGAAAGCATTTGCCAAGAAT - 3' and reverse primer 5' - GCATCGTTTATGGTCGGAAC - 3'.

1.5.7 Assay to determine if the neutralizing antibodies detach HAstV particles bound to cells

Confluent Caco-2 cell monolayers in 48-well plates were blocked with 1% BSA in PBS for 45 min at room temperature followed by a 15 min incubation on ice. Purified HAstV-1 or HAstV-2 particles were added at an MOI of 30 and then incubated for 1 h on ice to allow the binding of the virus to the cell surface. The unbound virus was subsequently removed by washing three times with cold PBS. Serial 1:5 dilutions of the indicated ascitic fluids of either 3B4 or 3H4 for HAstV1, or 4B6 for HAstV2 were added to the cells and then incubated for 1 h on ice. After this incubation, the antibody and detached virus were removed with cold PBS, and RNA extraction and

RT-qPCR quantification were performed as described above. MAb 2D9, which neutralizes HAstV8, was used as a negative control.

1.5.8 X-ray crystallography structure determination of HAstV2 spike/scFv 4B6 complex

Thrombin digestion was used to remove the Histidine-tag from HAstV2 spike and to remove the StrepII tag from scFv 4B6 with 10 U thrombin/mg of protein incubated at 4 °C on a rotating plane overnight. Digestion of StrepII tag from scFv 4B6 and Histidine-tag from HAstV2 spike was confirmed by SDS-PAGE where no visually detectable undigested product was observed. HAstV2 spike was complexed with 2X molar excess scFv 4B6 per spike monomer and the resulting complex was purified by size-exclusion chromatography on a Superdex 75 10/300 GL column. Fractions corresponding to HAstV2 spike/scFv 4B6 complex were determined by peak comparison with gel filtration standards (peak elution volume corresponding to ~100 kDa) and SDS-PAGE analysis. Fractions of purified HAstV2 spike/scFv 4B6 complex were pooled and concentrated to 5 mg/ml in TBS pH 8.5. HAstV2-spike/scFv 4B6 protein crystals were formed in 2 µl drops containing a 1:1 ratio of protein solution to well solution consisting of 0.1 M Tris-HCl pH 8.5, and 0.74 M sodium citrate pH 5.5, using hanging drop vapor diffusion at 22 °C. A single crystal was transferred into a cryoprotectant solution consisting of well solution and 18% glycerol, and was then flash-frozen into liquid nitrogen. The Advanced Photon Source synchrotron beamline 23-ID-D was used to collect a diffraction dataset with

wavelength 1.0332 Å at cryogenic temperatures. The dataset was processed and scaled using DIALS (ccp4i2) with a resolution cutoff of 2.67 Å based upon $CC_{1/2}$ and I/σl statistics. A trimmed model of HAstV2 spike (PDB: 3QSQ) and a trimmed model of scFv 4B6 generated by SWISS-model using tremelimumab Fab as a template (PDB: 5GGU) was used for molecular replacement with Phaser. The structure was then manually modeled using Coot and refined in Phenix. The final model was deposited into the Protein Data bank (PDB 9CN2).

1.5.9 Single-particle CryoEM structure determination of HAstV1 spike/Fab 3B4/Fab 3H4 complex

Thrombin digestion was used to remove the Histidine-tag from HAstV1 spike and remove the StrepII tags from Fab 3H4 and Fab 3B4 as described above. HAstV1 spike was complexed with 2X molar excess Fab 3B4 and the resulting complex was purified by SEC on Superdex 200 10/300 GL column. Fractions corresponding to the HAstV1 spike/Fab 3B4 complex were determined by peak comparison with molecular weight standards (peak elution volume corresponding to ~100 kDa) and SDS-PAGE analysis. These fractions were pooled, and the resulting complex was then mixed with 1.5X molar excess Fab 3H4 and purified by SEC on a Superdex 200 10/300 GL column. Fractions corresponding to the full HAstV1 spike/Fab 3B4/Fab 3H4 complex were determined by peak comparison with gel filtration standards (peak elution volume corresponding to ~200 kDa) and SDS-PAGE analysis. Fractions of purified HAstV1 spike/Fab 3H4/Fab 3B4 complex were pooled and concentrated to

0.86 mg/ml in 10 mM Tris pH 7.0 and 150 mM NaCl. 3 µl of protein complex was mixed with 0.5 µl of 25 µM lauryl maltose neopentyl glycol (LMNG) detergent to remove orientation bias and was then deposited onto glow discharged UltrAuFoil R.12/1.3 gold grids 400 mesh, blotted using a ThermoFisher Scientific (TFS) Vitrobot Mark IV at 4 °C and 100% humidity, and then plunge frozen into liquid ethane. Grids were screened at UCSC's Biomolecular CryoEM facility using a TFS Glacios 200 kV microscope coupled to a Gatan K2 Summit direct detector. The top-selected grids were then sent to the Pacific Northwest Center for Cryo-EM (PNCC) for data collection on a TFS Krios G3i microscope coupled to a Gatan K3 Biocontinuum Gif. 7,235 movies containing 60 frames each were collected using a pixel size of 0.415 Å/pixel in super-resolution mode (105,000 x) and an electron dose of 32.26 e/A^2. Movies were preprocessed (motion correction and CTF estimation) in CryoSPARC v4.3.2. Initial particle identification was performed using an unbiased blob picker, resulting in 4,132,753 particles, further extracted in a box size 686 pixels. After multiple rounds of 2D classification, 55 top-selected classes containing 214,273 particles underwent the *Ab-initio* reconstruction.

3 selected volumes were generated and then 3D-classified and further refined. The best-representing 3D class was used to create 2D references for a round of template picking. 2,718,470 particles were extracted with a box size 686 pixels, and then underwent on the similar previously established workflow. The top 72 classes containing 262,500 particles were used in a new *Ab-initio* reconstruction. The 2 generated classes were 3D-classified, where one class resulted in an overall gold-

standard resolution ($FSC_{0.143}$) of 5.70 Å and containing 138,147 particles. This volume was selected and underwent non-uniform refinement, and further non-uniform refinement using a mask encompassing the entire particle, resulting in a 3D reconstructed volume at 3.74 Å. Unused particles were added from the previous 2D classification, and all particles received local CTF refinement, resulting in a volume of 3.43 Å and 163,237 particles after non-uniform refinement. Additional rounds of local CTF refinement were performed and a mask in which the constant domains of the Fab were removed was used to align particles in local refinement, in order to improve the tridimensional alignment and local resolution of the epitope regions, resulting in the final reconstructed map at 3.33 Å overall resolution. The sharpened map (B factor -112 $Å^2$) was opened in ChimeraX (version 1.5.0) and starting models of the HAstV1 spike (PDB: 5EWO) and AlphaFold 3 models of Fabs 3H4 and 3B4 were fitted into the volume. Since the Fab constant domain volume density was poor, the constant domains were removed from the models. The initial model representing the complex was opened in Coot (version 0.9.1) and underwent several rounds of manual refinement and global real-space refinement and was validated using Phenix and MolProbity. The final reconstructed map was deposited in the Electron Microscopy Data Bank (EMD-45427) and the final model was deposited into the Protein Data Bank (PDB: 9CBN).

1.5.10 Biolayer interferometry K_D determination of neutralizing antibodies 3B4, 3H4, and 4B6:

Biolayer interferometry assays on an Octet RED384 instrument were used to determine binding affinity dissociation constants (K_D). Assays were performed in Octet Kinetics Buffer (PBS pH 7.4 + 0.1% BSA + 0.02% Tween 20) for Fabs 3H4 and 3B4, or Octet Kinetics Buffer + biocytin (PBS pH 7.4 + 0.1% BSA + 0.02% Tween 20 + 50 µM biocytin) for Fab 4B6. For assays with Fabs 3H4 and 3B4, pre-equilibrated Anti-Penta-His (HIS1K) biosensor tips were dipped into Octet Kinetics Buffer for 60 seconds for an initial baseline reading, dipped into 0.5 µg/ml histidine-tagged HAstV1 spike diluted in Octet Kinetics Buffer for 180 seconds to load the sensor tip, and dipped into Octet Kinetics Buffer for 60 seconds for a second baseline reading. Biosensors were then dipped into 4 serial dilutions of Fab in Octet Kinetics Buffer, consisting of 2.5 nM, 5 nM, 10 nM, and 20 nM for Fab 3H4, and 20 nM, 40 nM, 80 nM, 160 nM for Fab 3B4. This association step was run for 180 seconds, and then biosensors were dipped into Octet Kinetics Buffer to measure dissociation for a total of 600 seconds. For assays with Fab 4B6, pre-equilibrated Anti-Penta-His (HIS1K) biosensor tips were dipped into Octet Kinetics Buffer + biocytin for 60 seconds for an initial baseline reading, dipped into 0.5 µg/ml histidine-tagged HAstV2 spike diluted in Octet Kinetics Buffer + biocytin for 180 seconds to load the sensor tip, and dipped into Octet Kinetics Buffer for 60 seconds for a second baseline reading. Biosensors were then dipped into 4 serial dilutions of Fab 4B6 in Octet Kinetics Buffer, consisting of 25 nM, 50 nM, 100 nM, and 200 nM. This association step was run for 60 seconds, and then biosensors were dipped into Octet Kinetics Buffer to measure dissociation for a total of 60 seconds. These shorter association and

dissociation steps were chosen due to the lower affinity of the Fab 4B6. Kinetics data was processed the same way for all Fabs in the Data Analysis HT software. The baseline step was used to align traces and apply inter-step correction. A reference sample well containing only a spike-loaded biosensor dipped into no analyte (Fab) was subtracted. Savitzky-Golay filtering was used on the traces. For curve fitting, a 1:1 model was globally applied to the dilution series, and fit was evaluated based on R^2 and χ^2 values and visual inspection. Average K_D values are reported as the average of the three replicates.

1.5.11 Biolayer interferometry competition assay of Fabs versus FcRn for HAstV spike:

Biolayer interferometry competition assays were performed with an Octet RED384. Pre-equilibrated Streptavidin (SA) biosensors tips were dipped into Octet Kinetics Buffer for 60 seconds for an initial baseline reading. For Fabs 3H4 and 3B4, 0.5 µg/ml of biotinylated HAstV1 spike was loaded onto SA biosensors tips for 300 seconds, and dipped into Octet Kinetics Buffer for 30 seconds for a baseline reading. Biosensors were then dipped into either 150 nM Fab 3H4 or 250 nM Fab 3B4 in Octet Kinetics Buffer for 600 seconds to ensure saturation of all spike binding sites, dipped into Octet Kinetics Buffer for 30 seconds as a baseline reading, and then dipped into 2 µM FcRn in Octet Kinetics Buffer for 300 seconds. For Fab 4B6, the assay was performed with the same methods, but 0.5 µg/ml biotinylated HAstV2 spike was used during the antigen loading step, Octet Kinetics buffer + biocytin was

used for all assay steps after antigen loading, 250 nM Fab 4B6 was using during the antibody association step, and due to its lower affinity 250 nM of Fab 4B6 was also included in the baseline step after antibody association and in the FcRn sample to maintain saturation of Fab 4B6 on spike. All assays contained additional controls such as a sample in which the primary Fab was dipped into the same concentration of self Fab instead of FcRn to ensure that saturation was achieved, and also a control in which FcRn was bound to the HAstV spike in the absence of any Fab in the first association. All assays were performed in duplicate. Competition data was processed the same way for all Fabs in the Data Analysis HT software in the Epitope Binning module. A matrix representing competition was generated using the shift between the last 10% average of the signal from the second association and the last 10% average of the signal from the primary association step. The signal from the control in which primary Fab was dipped into self Fab for the second association was subtracted in the matrix row (the shift values from all samples containing the respective Fab), such that full competition is represented by "0." The signal from the control sample in which FcRn was associated to HAstV spike with no Fab in the primary association was used to normalize in the matrix column (the shift values from samples with FcRn binding in the secondary association step) such that maximum FcRn binding with no competition represents "1." This normalization is done separately for Fab 4B6 vs Fab 3H4 and 3B4 assays given the different spike serotypes that FcRn is associated to, but is displayed in the same table. Fabs were considered to compete with FcRn if FcRn

binding in the presence of Fab was reduced by 50% or more (a value of 0.5 or lower). The values shown are an average of duplicate assays.

1.5.12 scFv 3B4, scFv 3H4, and scFv 4B6 neutralization assays

The indicated concentration of antibody or scFv was preincubated with HAstV1 at an MOI of 0.02, for 1 h at room temperature. The virus-antibody mixture was then added to confluent Caco-2 cell monolayers grown in 96-well plates and incubated for 1 h at 37°C. After this time, the cells were washed three times with minimum essential medium (MEM) without serum, and the infection was left to proceed for 18 h at 37°C. Infected cells were detected by an immunoperoxidase focus-forming assay, as described previously. scFv 4B6 neutralization assays were performed the same way but using HAstV2.

1.6 Discussion

Here, we map three new epitopes on the HAstV spike that induce neutralizing antibodies, finding that 4B6 and 3B4 target the top of the spike in ways that are unique from previously characterized antibodies. Additionally, we find that 3H4 targets the base of the spike, representing an entirely unique epitope which is distant from previously characterized antibodies and targets mostly conserved residues. With these additional structures, we find that the majority of neutralizing antibodies target the upper side or top variable loop regions of the spike (Fig. 1.7). These regions

reside around conserved areas of the HAstV spike, termed the P-site and S-site, which were proposed as potential host protein interacting sites.[30] However, few of the antibody residues directly target these conserved sites. Although the direct receptor or host protein interaction locations on the spike are currently not known, it is likely that these neutralizing antibodies sterically hinder receptor binding to more functionally conserved regions located close by, rather than overlapping with receptor binding site(s) directly, given that the majority of neutralizing antibodies target highly variable loop residues on the top regions of the spike, indicating less functional importance for these residues. These loops may serve more as an immunogenic target for antibodies that can be more easily mutated without changing important functions of the spike. 3H4 represents an entirely new antigenic site near the base of the spike, which has less accessibility compared to the top exposed portion of the spike where the majority of antibodies target. This low epitope may have been favored more by recombinant spike vaccination than what would have been induced by the whole virus where the capsid core domain limits access. This suggests the possibility of using recombinant spike vaccinations for enhancing the induction of less accessible antigenic sites that may be more conserved on the spike, similar to how some recombinant influenza vaccine antigen candidates better elicit immune-subdominant hemagglutinin stem targeting antibodies. Given that 3H4 targets mostly conserved residues and has high affinity, it may have some potential as a monoclonal antibody therapy for HAstV2. However, 3H4 is vulnerable to mutations at residue K504, which additionally is not conserved between HAstV serotypes.

We find that all three antibodies, 3H4, 4B6, and 3B4, block binding of FcRn to the spike, although 3B4 only appears to partially block. From the structure, is can be seen that 3B4 leans more to one side of the spike dimer than the other. It is possible that this asymmetric nature of the 3B4 binding antibody could explain how only partial blocking of FcRn binding occurs if FcRn were to bind both sides of the spike homodimer and 3B4 was capable of only blocking one side. It is interesting that all three antibodies block FcRn binding given their different locations on the spike, which leads to our hypothesis that the blocking ability of these antibodies may be more related to steric hinderance and less related to where the antibodies bind directly. This does seem to be the case given that the scFvs of 3H4, 3B4, and 4B6 neutralize less effectively than full length mAb, however they are still able to neutralize virus at higher concentrations, indicating that there may still be some overlap with receptor-binding site(s), or that some steric hinderance still occurs with the variable region. Although all 3 antibodies appear to block binding of FcRn, it is unknown whether these antibodies could block other important host proteins such as the recently identified dipeptidyl peptidase-4 DPP4 receptor.[27] It is also possible that alternative mechanisms of neutralization could exist such as binding to prevent the proteolytic cleavage of immature HAstV into its infectious form, however this remains to be explored.

Overall, these studies further our structural and mechanistic understanding of neutralizing antibody epitopes on the HAstV capsid surface, supporting the rational design of vaccines that prevent childhood viral diarrhea by HAstV.

CHAPTER 2:

Structure and Immunogenicity of the Murine Astrovirus Capsid Spike

2.2 Acknowledgements

This chapter focuses on the development of a system in which to test spike-based vaccine antigens using Murine astrovirus (MuAstV) and mice as an animal model. This manuscript was published in the Journal of General Virology on November 1, 2023 under the title, "Structure and Immunogenicity of the Murine Astrovirus Capsid Spike," by Lanning S, Pedicino N, Haley DJ, Hernandez S, Cortez V, DuBois RM. My specific contributions to this work were designing the MuAstV spike construct, expression and purification of the MuAstV spike, running crystal trials with the MuAstV spike, collecting diffraction data, performing data processing and refinement for the final structure, running ELISAs with collected serum, and writing the first draft of the manuscript, further editing, and preparing figures. Natalie Pedicino performed vaccinations, sera collection, and qPCR on mice, DJ Haley ran an ELISA and helped prepare Figure 2.2, Sam Hernandez maintained mouse colonies, and Valerie Cortez and Rebecca M. DuBois conceptualized project ideas, supplied funding, supervised the work and edited the manuscript.

2.3 Abstract:

Human astroviruses are small, non-enveloped icosahedral RNA viruses that are a significant cause of diarrhea in young children. Despite their worldwide prevalence, HAstV pathogenesis studies and vaccine development remain challenging due to the lack of an animal model for HAstV infection. The recent development of a murine astrovirus infection model in mice provides the opportunity to test proof-of-concept vaccines based on MuAstV antigens. To help establish a system in which an astrovirus capsid spike-based vaccine could be tested in vivo, we designed and produced a recombinant MuAstV capsid spike protein based on predicted secondary structure homology to HAstV spike proteins. The recombinant MuAstV spike can be expressed with high efficiency in Escherichia coli and retains antigenicity to polyclonal antibodies elicited by MuAstV infection. We determined the crystal structure of the MuAstV spike to 1.75 Å and assessed its structural conservation with HAstV capsid spike. Despite low sequence identity between the MuAstV and HAstV spikes and differences in their overall shapes, they share related structural folds. Additionally, we found that vaccination with MuAstV spike induced anti-MuAstV-spike antibodies, highlighting that the recombinant spike is immunogenic. These studies lay a foundation for future in vivo MuAstV challenge studies to test whether MuAstV spike can be the basis of an effective vaccine.

2.4 Introduction:

Astroviruses are small, nonenveloped, single-stranded, positive-sense RNA viruses named after the 'star-like' appearance of their capsids from when they were first observed in human stool samples by electron microscopy in 1975.[32,33] Astroviruses infect a wide range of animal species in both birds and mammals, and mainly spread through the fecal–oral route. In humans, astroviruses are a leading cause of virus-induced diarrhea in young children, with similar disease severity to that caused by noroviruses.[1] Some studies show astrovirus infections in 2–15% of children hospitalized for diarrhea.[34,35,36] Human astroviruses infect most of the human population worldwide, with serology studies revealing that over 90% of adults have anti-HAstV antibodies from a prior infection, and that the presence of these antibodies is associated with a reduction in HAstV disease severity.[1,15,37,38,3] HAstV has eight known classical serotypes (HAstV1–8), with HAstV1 being the most common globally. More recently, divergent strains of HAstV from the VA/HMO and MLB clades have been discovered within the brain and cause fatal encephalitis in immunocompromised humans.[39,40,41] Despite the prevalence of HAstVs globally, much of their biology and pathogenesis remains unknown, in part due to the lack of an animal model in which to study HAstV infection in vivo. In the past, turkey poults and turkey astrovirus (TAstV) were used to study astrovirus pathogenesis.[42,43] However, turkey husbandry is difficult and turkey models have limited reagents and tools available.[44] Additionally, TAstV is phylogenetically distanced from HAstV,

being a part of the avian astrovirus genus, Avastrovirus, rather than the mammalian astrovirus genus, Mamastrovirus. Protein structural analyses have also revealed strong differences between the TAstV capsid spike domain compared to the HAstV capsid spike domain, suggesting that these two astroviruses may have different interactions with host proteins.[45] Therefore, the need for a more representative animal model system to study astrovirus pathogenesis in vivo is necessary. Recent efforts have focused on creating a model system for HAstV in mice using murine astrovirus (MuAstV). MuAstV was first discovered in murine stool samples by electron microscopy during an investigation of a diarrhea outbreak within a mouse colony in 1985[46] and has since been found in laboratory mice and wild mice worldwide.[47,48] MuAstV was not initially considered for an animal model over TAstV due to laboratory mice having a lack of diarrhea when experimentally infected with MuAstV – unlike turkeys, which experience diarrhoea when infected with TAstV shortly after hatching.[49] However, despite a lack of obvious clinical signs, MuAstV infection in mice presents a promising animal model with which to better understand HAstV infection. MuAstV is phylogenetically more similar to HAstV than TAstV and may consequently have more conserved viral mechanisms with HAstV. Additionally, mice have easier husbandry methods and more genetically engineered models and reagents that can be used to study astrovirus infection in vivo. MuAstV infection of live mice can be measured over time by qRT-PCR of stool samples, and some biological similarities have been implicated between MuAstV and HAstV, such as tissue tropism, cellular tropism and host responses to the virus.[48,50,51,52,53,54,55] However,

whether HAstV and MuAstV have similar virion structures remains unclear. The HAstV virion consists of a non-enveloped icosahedral capsid, ~40 nm across, sheltering a ~7 kb positive-sense ssRNA genome within the core. The T=3 virion capsid is made up of 180 subunits of the capsid protein, derived from the second genomic open reading frame (ORF2). Intracellular caspase proteolytic processing promotes cellular escape and extracellular proteolytic processing results in maturation into the infectious form.[19] The mature infectious form of HAstV contains an icosahedral shell formed by the capsid core domains with 30 homodimeric capsid spike domains protruding from the 2-fold icosahedral symmetry axes.[22] The HAstV capsid spike domain is thought to be responsible for attachment and entry of the virus.[28] Antibodies targeting the spike domain have been found to neutralize HAstV in cell culture.[25,24,56] While both the HAstV capsid core and spike domains are immunogenic, only antibodies to the spike domain are able to neutralize HAstV in cell culture, indicating the spike domain as a target for vaccine design.[25] To establish an in vivo model in which to study an astrovirus spike-based vaccine, we produced the recombinant MuAstV capsid spike protein, which can be expressed with high efficiency in Escherichia coli and retains antigenicity with anti-MuAstV antibodies. Additionally, we solved the high-resolution structure of the MuAstV spike, validating its folding and elucidating structural differences and similarities to the HAstV spike. Finally, we vaccinated mice with recombinant MuAstV spike protein and assessed antibody production and found that the MuAstV spike induces levels of anti-MuAstV

spike IgG antibodies that exceed those generated from natural infection. Our studies establish an in vivo system to study an astrovirus spike vaccine.

2.5 Results:

2.5.1 Production of recombinant MuAstV capsid spike protein

The MuAstV capsid spike sequence homology to HAstV capsid spike sequences is low (<18% amino acid identity), similar to the low homology between the capsid spikes from the three different HAstV clades (Fig. 1.1A,B). Reasoning that the spike domains would have structural homology, even in the absence of sequence homology, we used the HHPred server to predict MuAstV capsid secondary structural homology to HAstV1 and HAstV8 spike structures.[30] Based on this predicted secondary structure alignment, we designed a MuAstV spike expression plasmid to encode residues 428–676 from the capsid protein of MuAstV isolate SJ001 (Fig. 1.1C). The recombinant MuAstV spike protein expressed in E. coli had high expression and high solubility. The MuAstV spike has a calculated mass of 28 kD (+3 kD cleavable histidine affinity tag), which was validated by reducing SDS-PAGE (Fig. 1.1D). Size-exclusion chromatography revealed that the purified MuAstV spike protein eluted at an apparent molecular weight of 60 kD, indicating that the spike protein formed a dimer in solution, similar to all other known astrovirus spike proteins (Fig. 1.1E). These data, in conjunction with the X-ray crystallographic studies described below, confirm that the residues chosen for the recombinant

MuAstV spike construct represent accurate terminal boundaries of the MuAstV capsid spike domain.

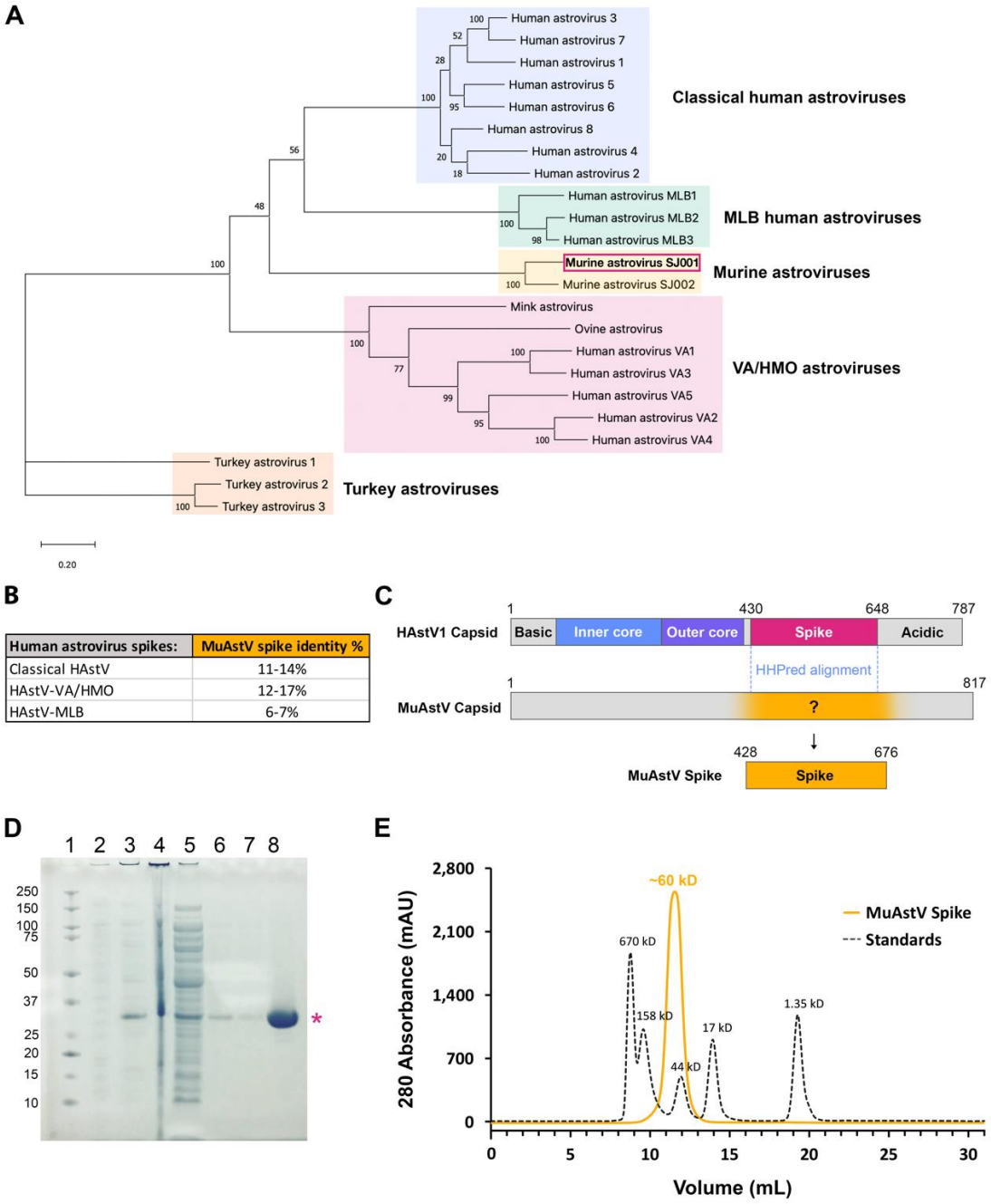

Figure 2.1: Elucidation of the MuAstV capsid spike domain boundaries

(A) Phylogenetic analysis of human astroviruses with several animal astroviruses. Analysis was performed using mega X with a muscle (EMBL-EBI) alignment of full-length ORF2 capsid protein sequences and the maximum-likelihood method and a JTT matrix-based model. The tree with the highest log likelihood (−27387.34) is shown. The tree was rooted using turkey astrovirus capsid proteins as an outgroup. **(B)** Pairwise amino acid sequence identities between MuAstV spike and the human astrovirus spikes, generated using muscle (EMBL-EBI) alignment. **(C)** Schematic of HHPred alignment prediction of the MuAstV spike domain. HAstV1 ORF2 capsid protein representation with known domains is shown above the MuAstV ORF2 capsid protein, with the subsequent residues chosen for the MuAstV spike domain based on an HHPred secondary structure alignment below. **(D)** SDS-PAGE analysis of *E. coli* expression and TALON purification of the MuAstV spike, which is indicated with an asterisk. Lane 1, BioRad Precision Plus molecular weight markers; lane 2, E. coli lysate pre-induction; lane 3, E. coli lysate postinduction; lane 4, E. coli insoluble pellet after lysis; lane 5, supernatant flow through after TALON bead incubation; lane 6, wash fraction; lane 7, final wash fraction; lane 8, purified MuAstV spike elution fraction. **(E)** Size-exclusion chromatography trace of MuAstV spike after histidine affinity tag removal and dialysis into TBS. The black dashed line represents gel filtration standards and the orange line represents the MuAstV spike.

2.5.2 ELISA assessment of recombinant MuAstV spike antigenicity

To validate that the recombinant MuAstV spike retains antigenic epitopes displayed on the native MuAstV virion, we tested whether antibodies in sera from mice infected with MuAstV isolate SJ001 could bind to the recombinant SJ001 MuAstV spike by ELISA. Mice were inoculated with faecal filtrate containing MuAstV, and infection was confirmed with qRT-PCR. Sera were collected 28 days post-infection. The IgG antibodies in polyclonal sera from MuAstV-infected mice showed a strong dosedependent response to the recombinant MuAstV spike domain by ELISA (Fig. 2.2A). Naïve mice showed virtually no reactivity (did not exceed

0.0829 absorbance at 490 nm), confirming specificity. These data support that recombinant MuAstV spike displays epitopes found on the native MuAstV virion.

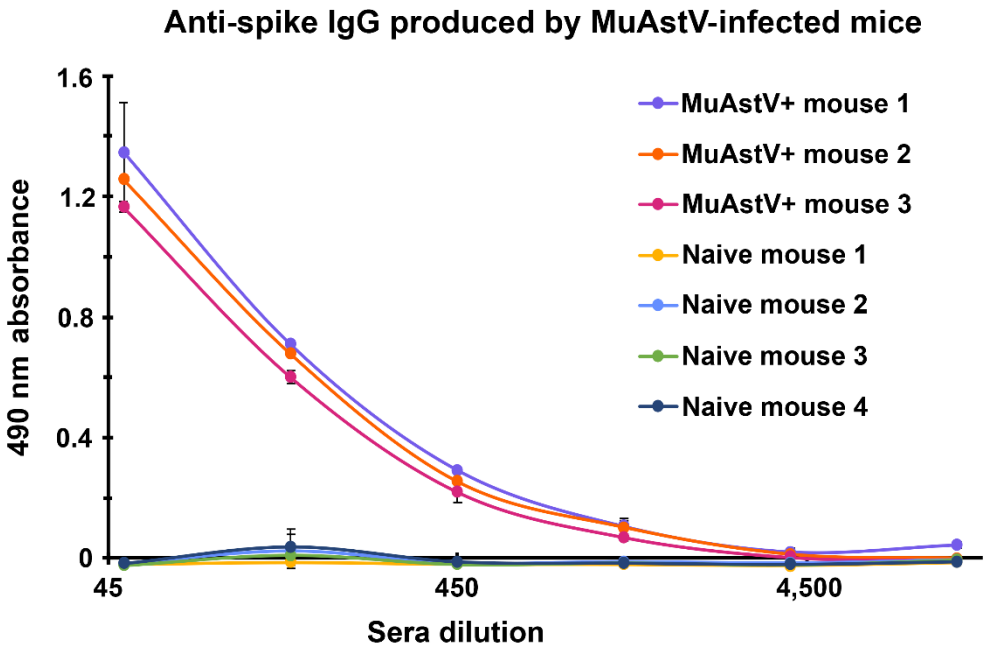

Figure 2.2: Recombinant MuAstV spike is antigenic and binds antibodies to native MuAstV

ELISA data showing that serum IgG antibodies from MuAstVinfected mice bind to the recombinant MuAstV spike protein. Naïve mice were not infected with MuAstV. Error bars represent one standard deviation away from mean absorbance of technical duplicates for each serum dilution tested. A matching negative control ELISA plate coated with BSA showed low or no reactivity (<0.11 absorbance at 490 nm), supporting the specificity of the ELISA

2.5.3 Crystal structure of MuAstV spike and comparison to HAstV spike

To further validate the folding of the recombinant MuAstV spike, we used X-ray crystallography to determine the MuAstV spike structure to 1.75 Å resolution (Fig. 2.3A, Table 2.1). Molecular replacement was successful using an AlphaFold2 model generated during the CASP15 competition after deletion of predicted loop

residues 441–465 and 564–596. Structural alignment of the experimentally determined MuAstV spike crystal structure with the AlphaFold2 model using TM-align resulted in an RMSD of 2.78 Å across 244 residue pairs and a TM score of 0.84754, revealing a relatively accurate match in the beta-strand regions but significant differences in several surface loops. The MuAstV spike crystal structure reveals a homodimeric protein (Fig. 2.3A), consistent with size-exclusion chromatography data, and confirms that the predicted MuAstV spike residues 428–676 form the domain. Interface analysis using the PDBePISA server revealed 1838 Å2 buried at the dimer interface, with 52–53 interacting residues in each chain (Fig. 2.3C). Similarly, the dimer interface of the HAstV1 spike is 1835 Å2, with 50 interacting residues in each chain (Fig. 2.3D). In addition, both the MuAstV spike and HAstV1 spike structures share an antiparallel beta-barrel fold with a similar folding topology found in all astrovirus spike structures (Fig. 2.3A, B). Despite these similarities, there are significant differences between MuAstV spike and HAstV1 spike structures. TM-align reveals an RMSD of 4.29 Å across 194 residue pairs and a TM-score of 0.66249. These structural differences result in different overall shapes and surfaces (Fig. 2.3C, D), most notably with the MuAstV spike containing a large cleft at the top, formed by the two long beta hairpins (β11–β12) from each protomer.

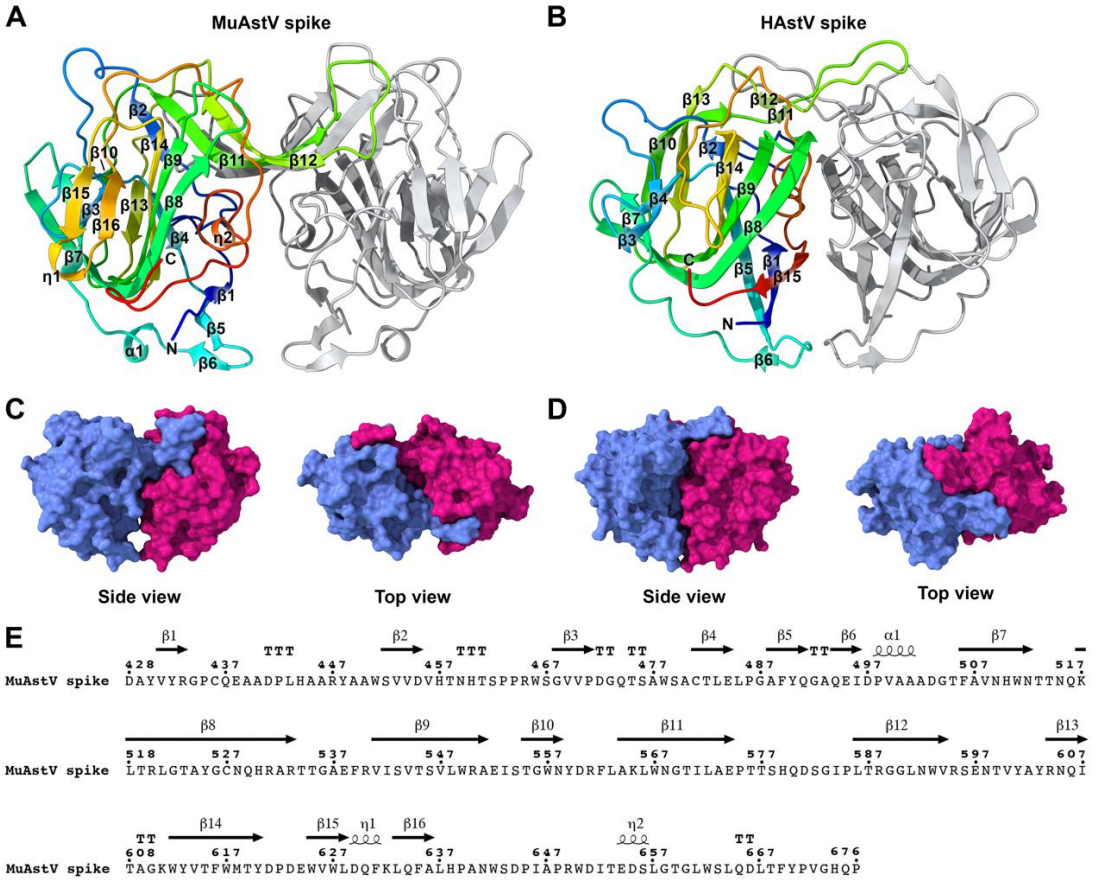

Figure 2.3: The MuAstV spike retains a similar folding topology to the HAstV spike but has differences in overall shape

(A) Side view of the MuAstV spike dimer presented as a cartoon model with labelled features on one protomer coloured rainbow from the N-terminus (blue) to the C-terminus (red). **(B)** Side view of the HAstV1 spike dimer (PDB : 5EW0) presented as a cartoon model. **(C)** Side and top views of the MuAstV spike dimer presented as a surface model with individual protomers coloured periwinkle and fuchsia. **(D)** Side and top views of the HAstV1 spike dimer (PDB : 5EW0). **(E)** Depiction of the secondary structural features of the MuAstV spike, displayed above the amino acid sequences where they occur.

Table 2. 1: Crystallographic statistics for MuAstV spike

Table 1. Data collection and refinement statistics	
	MuAstV spike (PDB: 8TN8)
Data collection:	
Wavelength (Å)	1.0332
Space group	P 1
Cell dimensions:	
a, b, c (Å)	45.3285, 48.8724, 65.4627
α, β, γ (°)	93.344, 102.906, 114.696
Resolution (Å)	43.75-1.75 (1.78-1.75)*
R_{merge}	0.048 (0.190)
I/σI	14.4 (1.9)
Completeness	94.79% (92.52%)
Multiplicity	1.7 (1.7)
$CC_{1/2}$	0.995 (0.936)
Refinement:	
Resolution (Å)	43.75-1.75 (1.813-1.75)
No. Reflections for refinement	45864
No. Reflections for R_{free}	2293
R_{work}/R_{free}	0.1706/0.2010
No. atoms	4339
Protein	4015
Ligand/Ion	2
Water	322
B -factors (Å^2):	27.11
Protein	26.68
Ligand/Ion	31.61
Water	32.41
RMSD:	
Bond lengths (Å)	0.005
Bond angles (°)	0.82
Ramachandran statistics:	
Favored (%)	97.6
Allowed (%)	2
Outliers (%)	0.4

**Values for the highest resolution shell are shown in parentheses*

Spherical densities larger than water molecules were observed associated with residues D623, D621 and N641 in both chains A and B (Fig. 2.4B). A potassium ion was modelled, as it was the best fit for CheckMyMetal parameters[57] in comparison to other ions of similar size or charge (Mg, Na, Ca) that were modelled and tested for coordination chemistry, agreement of experimental B-factors, occupancy and the metal binding environmental motif. Additionally, the crystallography condition in which the MuAstV spike crystallized included potassium formate, which could have been the source of the potassium ion. While this metal-binding site may be an artefact of crystallization conditions, it is intriguing to note that both aspartates are highly conserved amongst 15 MuAstV strains, suggesting possible functional importance (Fig. 2.4B).

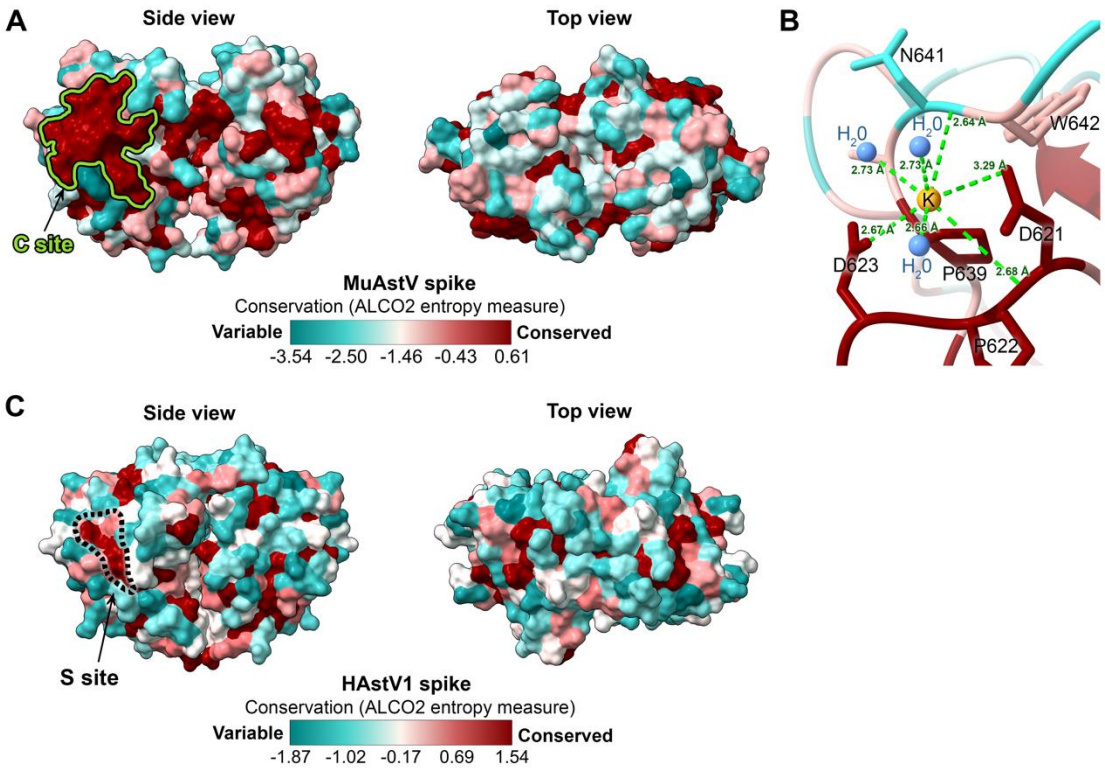

Figure 2.4: Conservation analysis of the MuAstV spike reveals a conserved region located on the side of the dimer, and high variability in the upper loop regions

(A) Side and top views of a conservation analysis of the MuAstV spike using 15 MuAstV strain sequences, colored with highly conserved residues in red, ranging to highly variable residues in teal. A conserved cluster, termed the 'C site', is indicated on the side view. **(B)** Crystal structure of the MuAstV spike with a potassium ion coordinated to MuAstV spike amino acid residues and water molecules. **(C)** Side and top views of a conservation analysis of the HAstV1 spike using sequences of the eight known classical serotypes (1–8), colored with highly conserved residues in red, ranging to highly variable residues in teal. A previously determined conserved cluster termed the 'S-site' is indicated on the side view.

2.5.4 Conservation analysis of the MuAstV spike

We further sought to identify which regions of the MuAstV spike may be functionally important by mapping conservation across 15 MuAstV sequences onto the MuAstV spike structure. A highly conserved patch of exposed residues (Q474-

S476, W511, Q529, R531, R533, W557, D621-D629, Q634, L637, Q675, P676) can be seen on one side of the spike protomer, as indicated by the C site in Fig. 4a. This site includes the potassium ion that was found coordinated with MuAstV spike residues D621, D623 and N641 and water molecules (Fig. 2.4B). Notably, this site is in a similar location to the relatively conserved S site on the side of the HAstV spike domain (Fig. 2.4C). Interestingly, within these sites there is short region of amino acids (WVW) that have conserved identity between HAstV and MuAstV. In the HAstV1 spike, this motif faces inward into the beta barrel, which indicates that the high conservation of this sequence is likely involved in the structural stability of the beta barrel core. In the MuAstV spike, the conserved WVW motif is more exposed, with these hydrophobic sidechains facing outward rather than inward, suggesting the possibility that they may be involved in a functional binding interface. Interestingly, the distinctive long beta hairpins (β11–β12) forming the top cleft of the MuAstV spike show higher variability than regions located on the sides of the spike.

2.5.5 Immunogenicity of MuAstV spike

To establish a system in which a spike-based vaccine immunogen could be tested in vivo, we assessed whether the recombinant MuAstV spike protein could induce anti-spike IgG antibodies in mice. Female littermates were vaccinated intraperitoneally with three doses of MuAstV spike every 2 weeks and tested for polyclonal anti-MuAstV spike IgG antibodies by ELISA using sera collected pre- and post-vaccination. Post-vaccinated sera showed strong anti-MuAstV spike IgG

responses (Fig. 2.5), indicating that the MuAstV spike protein is immunogenic. Interestingly, three of the four mice had stronger responses than MuAstV-infected mice, although the strength of the responses showed notable variation in individual mice.

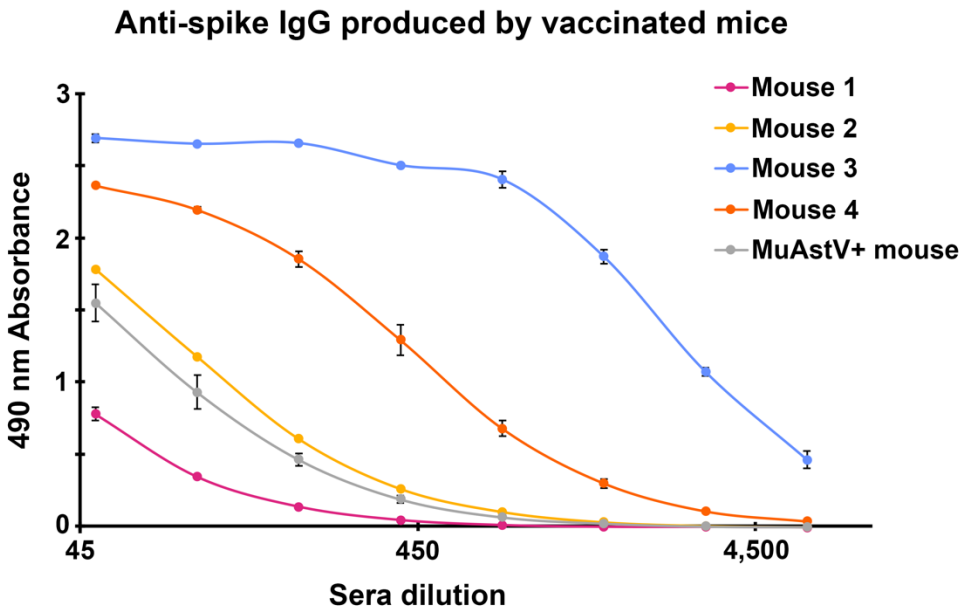

Figure 2.5: The MuAstV spike protein is immunogenic and induces anti-MuAstV spike IgG antibodies

ELISA data showing reactivity of IgG antibodies in vaccinated mouse sera to the MuAstV spike from four mice that were vaccinated intraperitoneally with MuAstV spike protein. Sera from a MuAstV seropositive mouse (described previously) were used as a positive control. Error bars represent one standard definition away from mean absorbance of technical duplicates for each sera dilution tested. A matching negative control ELISA plate coated with BSA showed low or no reactivity (<0.08 absorbance at 490 nm), supporting the specificity of the ELISA.

2.6 Materials and Methods:

2.6.1 Production of recombinant MuAstV capsid spike protein

The full-length open reading frame of MuAstV capsid protein (ORF2) originating from MuAstV strain SJ001 was retrieved from GenBank #MK395165.1. Known secondary structural features of HAstV1 and HAstV8 spike protein were aligned with secondary structure predictions for the full MuAstV capsid sequence using HHPred.[58] Based on this alignment, the cDNA for MuAstV capsid amino acids 428–676 was codon-optimized for E. coli and cloned into a pET52b vector in-frame with an N-terminal methionine and a C-terminal thrombin protease cleavage site and 10× histidine affinity tag (GenScript). This plasmid was transformed into E. coli strain T7 express (New England Biolabs) and grown in Luria broth (LB) with 50 μg ml−1 ampicillin. Expression of recombinant MuAstV spike was induced with 1 mM isopropyl-β-d-thiogalactopyranoside (IPTG) at 18°C and incubated overnight. E. coli cultures were centrifuged at 6000 g for 15 min, and the E. coli pellet was frozen at −20°C overnight. The next day, the E. coli pellet was resuspended in Buffer A (20 mM Tris–HCl pH 8, 20 mM imidazole, 500 mM NaCl), containing 1× EDTA-free protease inhibitors (EMD Millipore), benzonase (EMD Millipore #71205-25KUN) and 2.5 mM MgCl2 and was then lysed with ultrasonication. The lysate was centrifuged at 40000 g for 30 min and the supernatant was 0.22 μm filtered. Packed TALON beads prewashed with Buffer A were incubated with the filtered supernatant on a rotating plane at 4 °C for 1 h. The beads were then placed into a Bio-Spin Chromatography Column (Bio-Rad) and washed 6× with Buffer A. The MuAstV spike was eluted in Buffer B (20 mM Tris–HCl, 500 mM NaCl, 500 mM imidazole, pH 8). Yield was 18 mg of protein from a 1 liter expression. Purified MuAstV spike

protein was dialyzed into TBS (10 mM Tris–HCl pH 8, 150 mM NaCl) overnight at 4°C. The cleavable 10× histidine tag was removed from the MuAstV spike protein by incubation with bovine thrombin protease overnight on a rotating plane at 4°C. Cleaved 10× histidine tags were confirmed with SDS-PAGE, with cleavage efficiency near ~100%. The MuAstV spike protein was further purified by size exclusion chromatography (SEC) using a Superdex 75 10/300 GL column in TBS pH 8.

2.6.2 Structural determination of the MuAstV spike

Purified MuAstV spike protein was concentrated to 7 mg ml−1 in TBS. MuAstV spike protein crystals were formed in 0.4 µl drops containing a 1: 1 ratio of protein solution to well solution containing 0.2 M potassium formate pH 7.3 and 20% (w/v) PEG 3350, using sitting drop vapour diffusion at 22°C. A single crystal was transferred into a cryoprotectant solution consisting of 0.2 M potassium formate pH 7.3, 20% (w/v) PEG 3350 and 25% glycerol, and was then flash frozen into liquid nitrogen. The Advanced Photon Source Beamline 23-ID-D was used to collect a diffraction dataset with wavelength 1.033 Å at cryogenic temperatures. The dataset was processed and scaled using DIALS (ccp4i2) with a resolution cutoff of 1.75 Å. A trimmed model generated by AlphaFold 2 for the CASP15 competition was used for molecular replacement with Phaser. AutoBuild was used to build an initial model, which was then modelled manually using Coot[59] and refined in Phenix[60] for the final structure.

2.6.3 MuAstV infection and MuAstV spike vaccination studies in mice

Male and female wild-type C57BL/6 weanling mice (3–5 weeks old) were used for the infection studies. Mice were bred within the UCSC vivarium and housed in SPF conditions (n=5 mice/cage). Prior to experiments, animals were confirmed to be negative for MuAstV by qRT-PCR screening of fresh faeces. Briefly, faecal pellets were homogenized and supernatants clarified by centrifugation before RNA was extracted using the QiAmp Viral RNA Mini kit (Qiagen). Copies of the MuAstV genome were quantified using a g-block standard (Integrated DNA Technologies) in a one-step qRT-PCR using TaqMan Fast Advanced Master Mix Virus (Applied Biosystems) with primers (F: TACATCGAGCGGGTGGTCGC, R: GTGTCACTAACGCGCACCTTTTCA) and probe [(6-FAM)-TTTGGCATGTGGGTTAA-(MBGNFQ)] under the following conditions: 50 °C for 5 min and 95 °C for 20 s, followed by 40 cycles of 95°C for 3 s and 60°C for 30 s on a BioRad CFX96 Real Time System. Mice were inoculated orally with 100 µl of 0.22 µm filtered filtrate (100 mg ml−1), corresponding to 3.05×106 genome copies of MuAstV strain SJ001, and infection was confirmed by qRT-PCR. At 28 days post-infection, mice were euthanized by cardiac puncture for terminal blood collection. Blood samples were allowed to clot for 30 min at room temperature and then serum was collected by centrifugation at 2000 g for 15 min at 10°C. For vaccinations, female littermates were immunized intraperitoneally with 50 µg of MuAstV spike protein diluted 1: 1 in Complete Freund's Adjuvant (Sigma) for dose 1 followed by three doses in Incomplete Freund's Adjuvant (Sigma). Vaccinations were

administered every 2 weeks along with blood collection via submandibular puncture and then terminal bleeds as described above. Prior to vaccination, endotoxin was removed from MuAstV spike using 0.25 ml Pierce High-Capacity Endotoxin Removal Spin Column (Thermo Fisher #88273) using the batch method with a 4°C rotating overnight incubation of the MuAstV spike with the endotoxin removal resin.

2.6.4 Antigenicity studies of MuAstV spike using enzyme-linked immunosorbent assay (ELISA)

Ninety-six-well microtitre ELISA plates (Costar #3590) were coated with 50 µl of 2 µg ml−1 purified MuAstV spike in phosphatebuffered saline (PBS), covered with microplate sealing tape (Corning #6575) and incubated overnight at 4 °C. Plates were washed three times (200 µl each) with PBS-T (PBS+0.1% Tween) and dried on a kimwipe. Then 200 µl of blocking solution (PBST+5% milk) was added to all wells of the plate and incubated for 1h at room temperature. The blocking solution was thrown off the plate after incubation and tapped dry on a kimwipe. Then 80 µl of blocking solution was added to all wells. An extra 28 µl of blocking buffer was added to columns 1 and 2. Twelve microlitres of prediluted 1:5 sera from MuAstV-seropositive mice (see previous MuAstV infection methods) or prediluted 1:5 naïve sera was added to the first well in columns 1 and 2, and the remaining sera samples were added to each of the eight rows, making a 1:50 initial dilution on the plate. The multichannel pipette was used to pipette up and down four–six times in column 1 and to transfer 40 µl to column 3. This was repeated until column 11, and the last 40 µl

was discarded. The same dilution process was used from column 2 to column 12 to make duplicate dilutions. Plates were incubated with diluted sera at room temperature for 2 h. Plates were then washed three times with 200 µl PBS-T. Goat anti-mouse IgG-HRP secondary antibody (Jackson ImmunoResearch #115-035-071) was diluted 1: 3000 in PBS-T+1% milk and 50 µl was added to each well and incubated at room temperature for 1 h. After 1 h incubation, plates were washed three times with 200 µl PBS-T. Immediately before use, two tablets of OPD (Thermo #34006) and 12.5 µl of 30% hydrogen peroxide were added to 25 ml of 0.05 M phosphate citrate buffer (Sigma Aldrich #P4809). 100 µl was added to each well of the plate. Exactly 10 min after the OPD solution was added to the first row, 50 µl of 3M HCl was added to stop the reaction. ELISA plates were read in a plate reader at an absorbance of 490 nm. A control ELISA plate coated with 2 µg ml−1 bovine serum albumin (BSA) antigen was run with the same methods.

2.6.5 Immunogenicity studies of MuAstV spike using ELISA

Ninety-six-well microtitre ELISA plates (Costar #3590) were coated with 50 µl of 2 µg ml−1 purified MuAstV spike in PBS, covered with microplate sealing tape (Corning #6575) and incubated overnight at 4 °C. Plates were washed three times (200 µl each) with PBS-T and then dried on a kimwipe. Then 200 µl of blocking solution (PBS-T+5% milk) was added to all wells of the plate and incubated for 1 h at room temperature. The blocking solution was thrown off the plate after incubation and tapped dry on a kimwipe. Then 80 µl of blocking solution was added to all wells.

An extra 64 µl of blocking buffer was added to row A. Sixteen microlitres of prediluted 1: 5 sera from MuAstV spike-vaccinated mice (see previous MuAstV infection methods) was added to the first well in row A, and the remaining sera samples were added to each of the columns, making a 1: 50 initial dilution on the plate. The multichannel pipette was used to pipette up and down four–six times in row A and to transfer 80 µl to row B. This was repeated until row H, and the last 80 µl was discarded. Samples were run in duplicate across the columns. Plates were incubated with diluted sera at room temperature for 2 h. They were then washed three times with 200 µl PBS-T. Anti-mouse IgG-HRP secondary antibody (Jackson ImmunoResearch #115-035-071) was diluted 1: 3000 in PBS-T+1% milk and 50µl was added to each well and incubated at room temperature for 1 h. After 1 h incubation, plates were washed three times with 200 µl PBS-T. Immediately before use, two tablets of OPD (Thermo #34006) and 12.5 µl of 30% hydrogen peroxide were added to 25 ml of 0.05 M phosphate citrate buffer (Sigma-Aldrich #P4809). Then 100 µl was added to each well of the plate. Exactly 10 min after OPD solution was added to the first row, 50 µl of 3M HCl was added to stop the reaction. ELISA plates were read in a plate reader at an absorbance of 490 nm. A control ELISA plate coated with 2 µg ml−1 BSA was run with the same methods. ELISAs for naïve sera were run with similar methods, but could not be run in duplicate due to limited sera sample volume, and represent only a single replicate, and for particularly limited sera (mouse 4) the first sample dilution started at 1:100 rather than 1:50.

2.6.6 Phylogenetic analysis of astroviruses with MEGA X

Full astrovirus capsid ORF2 amino acid sequences were aligned using muscle (EMBL-EBI).[61] The following ORF2 sequences were used: human astrovirus 1, GenBank #AAC34717.1; human astrovirus 2, GenBank #Q82446.1; human astrovirus 3, Uniprot #Q9WFZ0.1; human astrovirus 4, Uniprot #Q3ZN05.1; human astrovirus 5, Uniprot #Q4TWH7.1; human astrovirus 6, Uniprot #Q67815.1; human astrovirus 7, Uniprot #Q96818.2; human astrovirus 8, Uniprot #Q9IFX1.2; human astrovirus MLB1, NCBI #YP_002290968.1; human astrovirus MLB2, GenBank #YP_004934010.1; human astrovirus MLB3, GenBank #YP_006905854.1; human astrovirus VA1, GenBank #YP_003090288.1; human astrovirus VA2, NCBI #ACX83591.2; human astrovirus VA3, NCBI #YP_006905860.1; human astrovirus VA4, NCBI #YP_006905857.1; human astrovirus VA5, GenBank #AJI44022.1; turkey astrovirus 1, GenBank #Q9JH68; turkey astrovirus 2, GenBank #Q9Q3G5; turkey astrovirus 3, GenBank #AY769616.1; mink astrovirus (mamastrovirus 10), GenBank #NC_004579.1; ovine astrovirus (mamastrovirus 13), GenBank #MK211323.1; murine astrovirus SJ002, GenBank #MK395166.1; murine astrovirus SJ001, GenBank #MK395165.1. An evolutionary history of astrovirus species was inferred using the maximum-likelihood method and a Jones–Taylor–Thornton (JTT) matrix-based model.[62] The tree with the highest log likelihood (−27387.34) is shown. The percentage of trees in which the associated taxa clustered together is shown next to the branches. Initial tree(s) for the heuristic search were obtained automatically by applying neighbour-joining and BioNJ algorithms to a matrix of pairwise distances

estimated using the JTT model, and then selecting the topology with superior log likelihood value. The tree is drawn to scale, with branch lengths measured in the number of substitutions per site. The tree was rooted using the turkey astroviruses as an outgroup. This analysis involved 23 amino acid sequences. There was a total of 920 positions in the final dataset. Evolutionary analyses were conducted in mega X.[63]

2.6.7 Pairwise identity analysis between MuAstV spikes and HAstV spikes

Pairwise identity between astrovirus spike sequences was calculated using muscle (EMBL-EBI) alignment. Accession numbers for MuAstV spike and the human astrovirus spikes were the same as those included in the phylogenetic analysis section. The following amino acid residues corresponding to spike domains within the ORF2 capsid protein were used: HAstV1, 431–644; HAstV2,429–644; HAstV3, 432–645; HAstV4, 430–644; HAstV5, 429–641; HAstV6, 430–642; HAstV7, 431–644; HAstV8, 490–705; HAstV-MLB1, 420–646; HAstV-MLB2, 417–643; HAstV-MLB3, 417–643; HAstV-VA1, 408–682; HAstV-VA2, 404–688; HAstV-VA3, 388–691; HAstV-VA4, 408–685; HAstV-VA5, 406–678.

2.6.8 Conservation analysis of MuAstV spike residues

Fifteen MuAstV ORF2 sequences were selected from the CLEAN_UNIPROT database using HMMER to search for unique nonredundant sequences between 15–99% identity to the spike from the SJ001 strain used for the MuAstV spike protein construct. The following MuAstV ORF2 sequences were used: A0A7G9ZE80,

A0A2S0SZ07, A0A866W0H6, A0A1Z2YAL6, A0A482N8A3, A0A866W226, K0BXK4, K0BZ51, K0C113, K0C109, A0A6B9KGG5, I3PL98, A0A482N9T7, R4MSW9 and A0A866W2R1. These sequences were aligned with the MuAstV spike sequence (amino acids 428–676, GenBank #MK395165.1) using muscle. Conservation was mapped in ChimeraX with a deep red colour representing the highest conserved residues for this alignment with an ALCO2 value of 0.61 between all 15 sequences and teal representing the maximum variable residues for this alignment with an ALCO2 value of −3.54.

2.6.9 Conservation analysis of HAstV1 spike residues

Eight HAstV sequences corresponding to the eight classical serotypes for HAstV1-8 were aligned using muscle and conservation was mapped onto the HAstV1 spike structure (PDB:5EW0). The following sequences were used for the alignment: human astrovirus 1, GenBank #AAC34717.1; human astrovirus 2, GenBank #Q82446.1; human astrovirus 3, Uniprot #Q9WFZ0.1; human astrovirus 4, Uniprot #Q3ZN05.1; human astrovirus 5. Uniprot #Q4TWH7.1; human astrovirus 6, Uniprot #Q67815.1; human astrovirus 7, Uniprot #Q96818.2; human astrovirus 8, Uniprot #Q9IFX1.2. Conservation was mapped in ChimeraX with a deep red colour representing the maximum conserved residues for this alignment with an ALCO2 value of 1.54 between sequences and teal representing the maximum variable residues for this alignment with an ALCO2 value of −1.87.

2.7 Discussion:

Here we delineated the boundaries of the recombinant MuAstV capsid spike domain and determined its structure to 1.75 Å resolution, providing information about its evolutionary and functional relationship with HAstV spike. Additionally, we validated that the recombinant MuAstV spike retains antigenicity to antibodies elicited by native MuAstV infection and demonstrated that it can induce robust anti-spike IgG antibodies in vivo. Although the sequence identity between the MuAstV spike and HAstV spike is low, the structural similarities between the two spikes remain more conserved. Similar to the capsid spikes of other astroviruses, the MuAstV spike forms a stable homodimer that is maintained by both hydrophilic and hydrophobic interactions in the dimer interface, as well as by the interactions of the long loops extending from the beta hairpin β11–β12 that overlap onto the top of the opposing protomer (Fig. 3). The dimer interface surface area of the MuAstV spike is remarkably similar to the interface surface area of HAstV1 spike, with a close number of interacting residues, indicating that the structural integrity of the dimer interaction is conserved between the HAstV1 and MuAstV spikes. Furthermore, the MuAstV spike retains an anti-parallel beta barrel at the core of each protomer, as seen in astrovirus spike proteins from other host species, such as HAstV and TAstV. One notable difference between the MuAstV spike structure and that of other astrovirus spikes is the presence of a 'cleft' formed by the two β11–β12 beta hairpins that run along the top of the dimer interface. Additionally, the hole near the base of the spike

between the two monomers is more pronounced in the MuAstV spike than in the HAstV spike. Together, these differences result in a different overall shape of the MuAstV spike compared to other astrovirus spikes. Alignment of the MuAstV spike crystal structure with the same corresponding residues of the AlphaFold 2 model using TM-align revealed a relatively accurate match.[64] The most distinct differences between the structures lay in the same loop residues that needed to be deleted in the AlphaFold 2 model for molecular replacement to succeed. Previous molecular replacement attempts using HAstV1 spike or a SWISS-MODEL-generated model of the MuAstV spike sequence in a HAstV1 spike template found no solution. These trials showed that predictive software such as AlphaFold 2 are better at predicting structure than template-based models in the case of divergent astrovirus spike proteins and therefore may be more useful for generating molecular replacement models for X-ray crystallography. Based on a sequence alignment of 15 MuAstV strains, a cluster of conserved residues is seen on the side of the MuAstV dimer, which is indicated by the C site in Fig. 4. It is unknown whether these conserved residues indicate a possible host interaction site, or whether this site is necessary for structural integrity. The C site encompasses a similar area on the MuAstV spike monomer face to the previously determined S site on the HAstV spike, a conserved region on the eight classical serotypes of HAstV, but is notably not observed on the divergent MLB spike.[30,65] Although the C site on the MuAstV spike is in a similar location to the S site on the classical HAstV spikes, most of the sequences differ from those on the S site, aside from the WVW amino acid motif (amino acids 625–627 on MuAstV

spike), and there is currently no evidence to suggest that they might interact with the same host factor. Despite this conserved motif, the MuAstV spike has lower similarity in sequence identity to all HAstV spikes (6–17% identity) than the divergent human MLB and VA strain spikes have with the classical HAstV spikes (21–26% identity).[65] The structure of the human VA spike remains unknown, but it is likely that it does not share sequence similarity with the conserved S-site, given its further divergence from the classical HAstV strains. The high variability at the top of the MuAstV spike in the β11–β12 hairpin and loop regions is also seen in HAstV spikes, and may indicate a more immunodominant region. In HAstV, this immunodominance is also evidenced by viral escape mutations located in the loop regions in the presence of previously characterized neutralizing monoclonal antibodies.[25] The SJ001 strain of MuAstV has a unique two-amino-acid deletion in relation to similar MuAstV strains between residues 535 and 536 (TTXXGAE) within the extended tip of the loop region of the β8–β9 hairpin, which suggests that this loop may also be under particular selective pressure. Interestingly, all previous structurally characterized neutralizing antibodies that target the HAstV spike have been found to predominantly target loop regions, and have also been shown to prevent the spike from attaching to cells,[28] likely by preventing receptor binding. The functional significance of the loops is not known, but given their high variability, their immunodominance could potentially aid the virus by drawing antibodies towards regions of the spike in which the virus can readily mutate without significant consequence to escape neutralization, unlike a functional receptor-binding domain, which faces selective pressure to remain

conserved to maintain viral fitness. A potassium ion was found in the MuAstV spike structure, with associated residues D621, D623 and N641 being highly conserved across MuAstVs. While the N641 residue is not highly conserved, the interaction with the potassium ion is facilitated by the backbone carboxyl oxygen and not the sidechain, so this residue may not need to be conserved in order to maintain an interaction with the potassium. The observation of this potassium ion may be biologically relevant, or it could be a matter of promoting protein crystallization. The recombinant MuAstV spike produced here represents the first production of the MuAstV spike domain alone to our knowledge, and reflects the native spike domain as assessed by its ability to bind anti-MuAstV antibodies and by its structure. Despite being expressed in a non-native host, the E. coli-produced recombinant MuAstV spike retains antigenic epitopes of the native MuAstV spike, similar to what has been seen with HAstV spikes, as well as previously made MuAstV ORF2 capsid constructs such as MuAstV VP70, VP34 and VP27.[66] A previous study predicted the MuAstV spike, VP25, as amino acids 421–681 of MuAstV ORF2 from the STL1 strain (UniProt K0C109), which is similar but larger than the spike domain boundaries determined here, consisting of amino acids 428–676 from the SJ001 strain (corresponding to amino acids 428–678 in the STL1 strain, due to the two-amino-acid deletion in the β9–β9 hairpin loop in the SJ001 strain).[66] The determination of the MuAstV spike domain boundaries could allow for easier serological surveillance of MuAstV in vivariums, given the high expression and solubility of the spike domain when expressed, and by providing an alignment template for different MuAstV

strains. We vaccinated mice with recombinant MuAstV spike and show that it is immunogenic and induces anti-spike IgG antibodies. These data, in conjunction with previous mouse vaccinations with recombinant HAstV spike, show that recombinant astrovirus spikes are able to induce anti-spike IgG antibody responses. Although it is currently unknown if the anti-MuAstV spike IgG antibodies are neutralizing (there is not yet an in vitro MuAstV infection model to test them), it has previously been shown that antibodies elicited by vaccination with recombinant HAstV spike are capable of neutralizing HAstV in cell culture and can also block HAstV spike attachment to human Caco2 cells.[28,25] Notably, we show that recombinant MuAstV spike vaccination can induce higher levels of anti-spike IgG antibody than MuAstV infection in vivo, as was seen in three of the four mice tested, which presents promising potential to immunize mice against MuAstV using a recombinant spike-based vaccine. Overall, these studies provide a foundation for future proof-of-concept studies to evaluate the ability of MuAstV spike-focused vaccine candidates to protect against MuAstV infection. Future studies may explore different recombinant MuAstV spike doses, adjuvants and routes of vaccination for the ability to protect against infection. Moreover, while we provide strong evidence for the immunogenicity of recombinant MuAstV spike protein, other platforms for spike antigen presentation, including mRNA and viral vectored platforms, such as the recently described rotavirus vaccine-vectored method,[67] could be explored. The MuAstV spike construct we produce here expresses with very high efficiency and could be scaled for mass production, either for use in serology assays or as a vaccine antigen. Our work also

provides information about the structural relationships between MuAstV spike and HAstV spike, which could be useful for determining evolutionary relationships, potential cross-species transmission mechanisms, or to further explore the biology of MuAstV infection.

APPENDIX 1:

HAstV8 Neutralizing Antibodies 2D9 and 3E8 Block Spike Attachment to Cells

A1.1 Acknowledgements:

This manuscript was published in the Journal of General Virology on November 1, 2022 under the title, "Structures of Two Human Astrovirus Capsid/Neutralizing Antibody Complexes Reveal Distinct Epitopes and Inhibition Virus Attachment to Cells," by Ricemeyer L, Aguilar-Hernández N, López T, Espinosa R, Lanning S, Mukherjee S, Cuellar C, López S, Arias CF, DuBois RM. My specific contributions to this work were developing a fluorescence microscopy assay, including cloning and expressing a GFP-HAstV8 spike, and developing a spike-cell attachment assay with Caco-2 cells, including optimizing sample incubation times and temperature, concentrations of antibody and GFP-HAsV8 spike samples, and cell fixation.

A1.2 Introduction:

Previously, our lab generated a panel of IgG1 monoclonal antibodies (mAbs), two of which were found to neutralize HAstV8 (mAbs 2D9 and 3E8).[25] However, the precise mechanism of how these antibodies were able to neutralize HAstV8 were not known. To explore how these antibodies neutralize, we developed a fluorescence microscopy assay to determine whether or not these neutralizing antibodies could block a fluorescent HAstV8 spike from binding to Caco-2 cells. Additionally, there is currently only a small amount of evidence indicating the HAstV spike protein as a viral attachment protein, so this is assay also seeks to support the characterization of spike as an attachment protein by showing that GFP-HAstV8 spike attaches to cells.

A1.3 Results:

A1.3.1 Antibodies 3E8 and 2D9 block attachment of GFP-HAstV8 spike to Caco-2 cells

To test if the human astrovirus capsid spike alone is sufficient for cell attachment and to show that antibodies block this attachment, we examined both the capacity of a recombinantly expressed green fluorescent protein GFP-HAstV8 spike fusion protein to attach to Caco-2 cells and the ability of Fabs 3E8 and 2D9 to prevent this attachment. We chose Fab constructs for this set of experiments to avoid the possible dimerization effect of MAbs and (occasionally) scFvs, which could potentially cause

cross-linking issues with dimeric GFP-HAstV8 spike. Caco-2 cells grown on glass coverslips were incubated with GFP alone, GFP-HAstV8 spike alone, or GFP-HAstV8 spike with Fab 3E8, 2D9, or 3B4. Cells were washed, fixed, and imaged by fluorescence microscopy. As shown in Fig. 6, Caco-2 cells incubated with phosphate-buffered saline (PBS) alone or with GFP alone had little to no green signal (Fig. A1.1A and B). In contrast, Caco-2 cells incubated with GFP-HAstV8 spike had bright green punctate patterns that appeared at or near the cell membranes (Fig. A1.2C). Furthermore, cells incubated with GFP-HAstV8 spike and either Fab 3E8 or Fab 2D9 had minimal puncta (Fig. A1.1D and E), suggesting that the Fabs specifically blocked HAstV8 spike attachment to cells. The negative control Fab 3B4 did not block attachment (Fig. A1.1F). These data reveal that the human astrovirus capsid spike alone is sufficient for cell attachment and that antibodies 3E8 and 2D9 are able to preclude virus attachment by specifically blocking the spike.

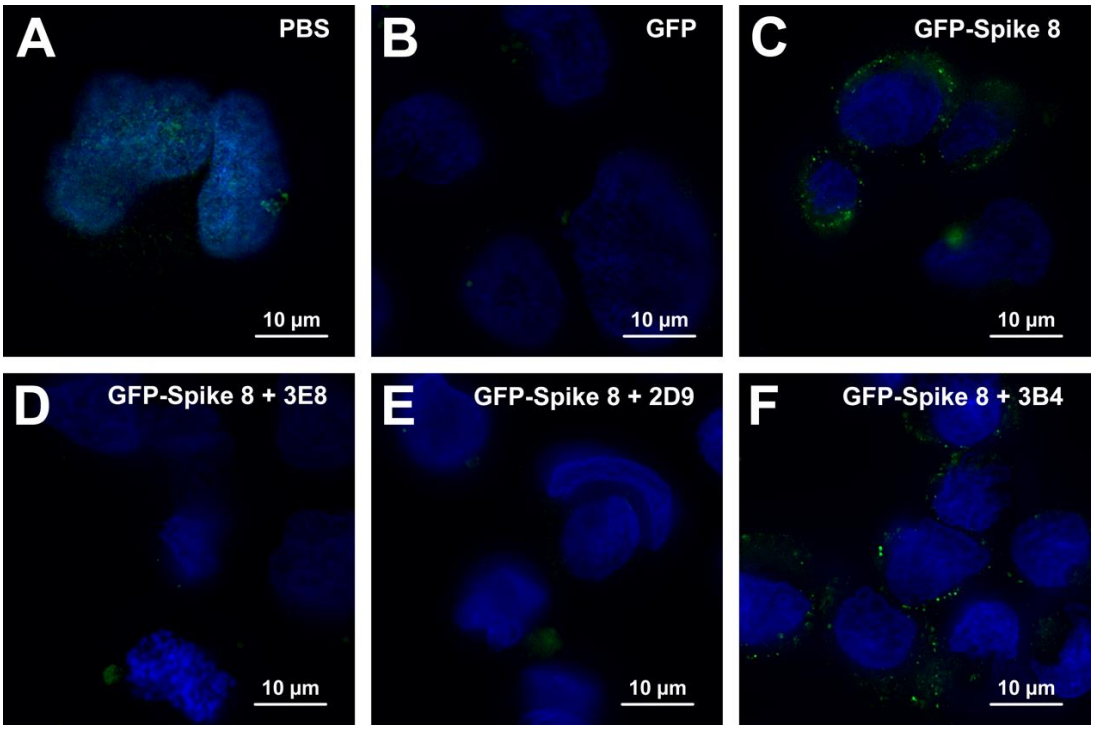

Figure A.1.3.1 Antibodies 3E8 and 2D9 block GFP-HAstV8 spike attachment to Caco-2 cells

GFP fluorescence is green and Hoechst DNA stain is blue. **(A)** Caco-2 cells incubated with PBS show slight autofluorescence. **(B)** Caco-2 cells incubated with GFP alone show little to no non-specific GFP binding. **(C)** Caco-2 cells incubated with GFP-HAstV8 spike show bright punctate patterns at or near the cell membranes, suggesting spike-specific attachment. **(D)** Fab 3E8 blocks GFP-HAstV8 spike attachment to Caco-2 cells. **(E)** Fab 2D9 blocks GFP-HAstV8 spike attachment to Caco-2 cells. **(F)** Fab 3B4 does not block GFP-HAstV8 spike attachment to Caco-2 cells.

A1.4 Materials and Methods:

A1.4.1 Expression and purification of chimeric Fabs 3E8, 2D9, and 3B4

Synthetic cDNA encoding the kappa and heavy chain variable regions of each antibody was cloned by Gibson Assembly into the pCMV-VRC01 antibody vectors

for light and heavy chains, in place of the variable regions of antibody VRC01, a human anti-HIV gp120 antibody. For the Fab heavy chain, only the variable region followed by the constant heavy 1 region ending with residues DKKVEPKSC was included, followed by an AS linker, C-terminal thrombin cleavage site, and a Twin Strep-tag. Sequences were in frame with the N-terminal signal sequence. The resulting chimeric Fab expression plasmids pCMVFab_kappa and pCMV-Fab_heavy_VH1CH1 (where Fab is 3E8, 2D9, or 3B4) contained both the variable regions from the original mouse antibodies and the constant regions from the human IgG1 antibody under the control of the human cytomegalovirus promoter. The plasmids were verified by DNA sequencing. The expression plasmids were used at a 3:2 ratio of kappa chain: heavy VH 1 CH1 chain to electroporate Chinese Hamster Ovary suspension (CHO-S) cells using the MaxCyte system. Recombinant chimeric Fabs were expressed for either 9 days (Fabs 3E8 and 3B4) or 7 days (Fab 2D9) by CHO-S cells, which were grown in CD OptiCHO expression medium supplemented with 1 mM sodium butyrate, 8mML-glutamine, 1X HT supplement, and 0.1% Pluronic F68 at 32°C with 125-rpm shaking. Every 24 h, cells were fed with CHO CD EfficientFeed A supplemented with 7 mM L-glutamine, 5.5% glucose, and 23.4 g/liter yeastolate. After 9 days, the cells were pelleted and medium containing secreted Fabs was 0.22-mm filtered, buffered to Strep wash buffer (50 mM Tris [pH 7.5], 150 mM NaCl, 1 mM EDTA), and supplemented with BioLock (IBA Lifesciences) to mask free biotin in the medium. The samples were 0.22-mm filtered again, affinity purified on two tandem 5-ml StrepTrap HP columns (GE), and eluted

in Strep elution buffer (Strep wash buffer with 2.5 mM desthiobiotin). Fabs 3E8 and 3B4 were dialyzed overnight into TBS (10 mM Tris-HCl [pH 7.2], 150 mM NaCl). Fab 2D9 was dialyzed overnight into 1X PBS (pH 7.4; Sigma-Aldrich).

A1.4.2 GFP-HAstV8 spike attachment inhibition assay by fluorescence microscopy

GFP-HAstV8 spike was expressed and purified as described previously (42). 24-well plates containing fibronectin-treated glass coverslips were seeded with 100,000 Caco-2 cells per well and allowed to adhere overnight. 250-ml samples containing 400 nM GFP-HAstV8 spike were incubated with 3 molar excess (1,200 nM) of Fabs of the HAstV8 spike-specific monoclonal antibodies 3E8 and 2D9 and the Fab of the HAstV1 spike-specific monoclonal antibody 3B4 for 1 h at room temperature in Dulbecco's phosphate-buffered saline (PBS; Gibco). Samples of PBS alone and 400 nM GFP were used as controls for autofluorescence and nonspecific binding, respectively. Media was aspirated from the cell monolayer, and then spike-Fab mixtures were added to Caco-2 cells and incubated at 4°C for 1 h. Protein mixtures were removed, and cells were washed with PBS and fixed with 2% paraformaldehyde (Thermo Fisher) in PBS for 15 min. Cells were washed with PBS and then stained with Hoechst 33342 dye (Thermo Fisher) in PBS for 30 min. Coverslips were washed with PBS, dried, and mounted in Vectashield mounting media on glass microscope slides. Z-stack images were acquired by using identical acquisition parameters with a Zeiss Axio Imager equipped with an AxioCam 506 monochrome camera using an oil-

immersion 100X/1.4 NA Plan Apo objective lens. Z-stack images contained 9 slices at 0.24-mm intervals, with GFP and Hoechst channels exposed for 1,600 and 95 ms, respectively. GFP signal was collected with a Zeiss Fset38 filter cube, and Hoechst signal was collected with a Zeiss Fset49 filter cube. After acquisition, images were deconvolved with AutoQuant X 3D deconvolution software (Media Cybernetics Version X3.1.3) for 10 iterations, using the Z-montage option. After deconvolution, a median filter with a 2-pixel kernel size was applied to the GFP channel of all images to reduce noise. Linear histogram adjustments were made to the GFP channel using FIJI,[68] such that minimum values were 1,300 and maximum values were 7,500, to help reduce background fluorescence. Single Z-stack slices from representative images were then converted to a single RGB image. Images were cropped to identical sizes in FIJI to select representative cells and are representative of data from at least three independent experiments.

References:

1. Olortegui, M. P. *et al.* Astrovirus Infection and Diarrhea in 8 Countries. *Pediatrics* **141**, e20171326 (2018).
2. Ghosh, S. *et al.* Enteric viruses replicate in salivary glands and infect through saliva. *Nature* **607**, 345–350 (2022).

3. Kurtz, J. B., Lee, T. W., Craig, J. W. & Reed, S. E. Astrovirus infection in volunteers. *J. Med. Virol.* **3**, 221–230 (1979).
4. Daniel-Wayman, S., Fahle, G., Palmore, T., Green, K. Y. & Prevots, D. R. Norovirus, astrovirus, and sapovirus among immunocompromised patients at a tertiary care research hospital. *Diagn. Microbiol. Infect. Dis.* **92**, 143–146 (2018).
5. Osborne, C. M., Montano, A. C., Robinson, C. C., Schultz-Cherry, S. & Dominguez, S. R. Viral gastroenteritis in children in Colorado 2006–2009. *J. Med. Virol.* **87**, 931–939 (2015).
6. Wunderli, W. *et al.* Astrovirus Infection in Hospitalized Infants with Severe Combined Immunodeficiency after Allogeneic Hematopoietic Stem Cell Transplantation. *PLoS ONE* **6**, e27483 (2011).
7. Black, R. E. *et al.* Estimated global and regional causes of deaths from diarrhoea in children younger than 5 years during 2000–21: a systematic review and Bayesian multinomial analysis. *Lancet Glob. Health* **12**, e919–e928 (2024).
8. The MAL-ED Network Investigators *et al.* The MAL-ED Study: A Multinational and Multidisciplinary Approach to Understand the Relationship Between Enteric Pathogens, Malnutrition, Gut Physiology, Physical Growth, Cognitive Development, and Immune Responses in Infants and Children Up to 2 Years of Age in Resource-Poor Environments. *Clin. Infect. Dis.* **59**, S193–S206 (2014).
9. Lee, T. W. & Kurtz, J. B. Human astrovirus serotypes. 2.
10. Jeong, H. S., Jeong, A. & Cheon, D.-S. Epidemiology of astrovirus infection in children. *Korean J. Pediatr.* **55**, 77 (2012).

11. Tao, Z. *et al.* Detection of multiple human astroviruses in sewage by next generation sequencing. *Water Res.* **218**, 118523 (2022).

12. Vu, D.-L., Cordey, S., Brito, F. & Kaiser, L. Novel human astroviruses: Novel human diseases? *J. Clin. Virol.* **82**, 56–63 (2016).

13. Lu, R. *et al.* The first evidence of shaking mink syndrome-astrovirus associated encephalitis in farmed minks, China. *Transbound. Emerg. Dis.* **69**, 3979–3984 (2022).

14. Comeau, D., Spinato, M. T., Ojkic, D., Foster, R. A. & Caswell, J. L. Bovine astrovirus and its role in lymphocytic encephalitis in cattle in Ontario, Canada, 1988–2019. *J. Vet. Diagn. Invest.* **36**, 447–456 (2024).

15. Meyer, L., Delgado-Cunningham, K., Lorig-Roach, N., Ford, J. & DuBois, R. M. Human Astrovirus 1–8 Seroprevalence Evaluation in a United States Adult Population. *Viruses* **13**, 979 (2021).

16. Koopmans, M. P. G., Bijen, M. H. L., Monroe, S. S. & Vinjé, J. Age-Stratified Seroprevalence of Neutralizing Antibodies to Astrovirus Types 1 to 7 in Humans in The Netherlands. *Clin. Diagn. Lab. Immunol.* **5**, 33–37 (1998).

17. Farahmand, M. *et al.* Worldwide prevalence and genotype distribution of human astrovirus in gastroenteritis patients: A systematic review and meta-analysis. *Microb. Pathog.* **181**, 106209 (2023).

18. York, R. L. *et al.* Structural, Mechanistic, and Antigenic Characterization of the Human Astrovirus Capsid. *J. Virol.* **90**, 2254–2263 (2016).

19. Banos-Lara, Ma. del R. & Méndez, E. Role of individual caspases induced by astrovirus on the processing of its structural protein and its release from the cell through a non-lytic mechanism. *Virology* **401**, 322–332 (2010).

20. Méndez, E., Fernández-Luna, T., López, S., Méndez-Toss, M. & Arias, C. F. Proteolytic Processing of a Serotype 8 Human Astrovirus ORF2 Polyprotein. *J. Virol.* **76**, 7996–8002 (2002).

21. Bass, D. M. & Qiu, S. Proteolytic Processing of the Astrovirus Capsid. *J. Virol.* **74**, 1810–1814 (2000).

22. Dryden, K. A. *et al.* Immature and Mature Human Astrovirus: Structure, Conformational Changes, and Similarities to Hepatitis E Virus. *J. Mol. Biol.* **422**, 650–658 (2012).

23. Aguilar-Hernández, N., López, S. & Arias, C. F. Minimal capsid composition of infectious human astrovirus. *Virology* **521**, 58–61 (2018).

24. Bass, D. M. & Upadhyayula, U. Characterization of human serotype 1 astrovirus-neutralizing epitopes. *J. Virol.* **71**, 8666–8671 (1997).

25. Espinosa, R. *et al.* Isolation of Neutralizing Monoclonal Antibodies to Human Astrovirus and Characterization of Virus Variants That Escape Neutralization. *J. Virol.* **93**, e01465-18, /jvi/93/2/JVI.01465-18.atom (2018).

26. Haga, K., Takai-Todaka, R., Kato, A., Nakanishi, A. & Katayama, K. *Neonatal Fc Receptor Is a Functional Receptor for Human Astrovirus*. http://biorxiv.org/lookup/doi/10.1101/2022.11.13.516297 (2022) doi:10.1101/2022.11.13.516297.

27. Ingle, H. *et al.* The neonatal Fc receptor and DPP4 are human astrovirus receptors. Preprint at https://doi.org/10.1101/2024.07.12.603331 (2024).

28. Ricemeyer, L. *et al.* Structures of Two Human Astrovirus Capsid/Neutralizing Antibody Complexes Reveal Distinct Epitopes and Inhibition of Virus Attachment to Cells. *J. Virol.* **96**, e01415-21 (2022).

29. Bogdanoff, W. A. *et al.* Structure of a Human Astrovirus Capsid-Antibody Complex and Mechanistic Insights into Virus Neutralization. *J. Virol.* **91**, e01859-16, e01859-16 (2017).

30. Dong, J., Dong, L., Méndez, E. & Tao, Y. Crystal structure of the human astrovirus capsid spike. 6.

31. Abramson, J. *et al.* Accurate structure prediction of biomolecular interactions with AlphaFold 3. *Nature* **630**, 493–500 (2024).

32. Madeley, C. R. & Cosgrove, B. P. VIRUSES IN INFANTILE GASTROENTERITIS. *The Lancet* **306**, 124 (1975).

33. Arias, C. & DuBois, R. The Astrovirus Capsid: A Review. *Viruses* **9**, 15 (2017).

34. Gaggero, A. *et al.* Prevalence of Astrovirus Infection among Chilean Children with Acute Gastroenteritis. *J. Clin. Microbiol.* **36**, 3691–3693 (1998).

35. Palombo, E. A. & Bishop, R. F. Annual incidence, serotype distribution, and genetic diversity of human astrovirus isolates from hospitalized children in Melbourne, Australia. *J. Clin. Microbiol.* **34**, 1750–1753 (1996).

36. Shastri, S., Doane, A. M., Gonzales, J., Upadhyayula, U. & Bass, D. M. Prevalence of Astroviruses in a Children's Hospital. *J. Clin. Microbiol.* **36**, 2571–2574 (1998).

37. Koopmans, M. P. G., Bijen, M. H. L., Monroe, S. S. & Vinjé, J. Age-Stratified Seroprevalence of Neutralizing Antibodies to Astrovirus Types 1 to 7 in Humans in The Netherlands. *Clin. Diagn. Lab. Immunol.* **5**, 33–37 (1998).

38. Kurtz, J. & Lee, T. Astrovirus gastroenteritis age distribution of antibody. *Med. Microbiol. Immunol. (Berl.)* **166**, 227–230 (1978).

39. Quan, P.-L. *et al.* Astrovirus Encephalitis in Boy with X-linked Agammaglobulinemia. *Emerg. Infect. Dis.* **16**, 918–925 (2010).

40. Brown, J. R. *et al.* Astrovirus VA1/HMO-C: An Increasingly Recognized Neurotropic Pathogen in Immunocompromised Patients. *Clin. Infect. Dis.* **60**, 881–888 (2015).

41. Cordey, S. *et al.* Astrovirus MLB2, a New Gastroenteric Virus Associated with Meningitis and Disseminated Infection. *Emerg. Infect. Dis.* **22**, 846–853 (2016).

42. Koci, M. D. *et al.* Astrovirus Induces Diarrhea in the Absence of Inflammation and Cell Death. *J. Virol.* **77**, 11798–11808 (2003).

43. Koci, M. D., Kelley, L. A., Larsen, D. & Schultz-Cherry, S. Astrovirus-Induced Synthesis of Nitric Oxide Contributes to Virus Control during Infection. *J. Virol.* **78**, 1564–1574 (2004).

44. Cortez, V. *et al.* Astrovirus Biology and Pathogenesis. *Annu. Rev. Virol.* **4**, 327–348 (2017).

45. DuBois, R. M. *et al.* Crystal Structure of the Avian Astrovirus Capsid Spike. *J. Virol.* **87**, 7853–7863 (2013).

46. Hem, Elisabet. Kjeldsbe. A. Detection of astroviruses in gut contents of nude and normal mice.

47. Ricart Arbona, R. J. *et al.* Serendipitous Discovery of a Novel Murine Astrovirus Contaminating a Murine Helper T-cell Line and Incapable of Infecting Highly Immunodeficient Mice. *Comp. Med.* **70**, 359–369 (2020).

48. Yokoyama, C. C. *et al.* Adaptive Immunity Restricts Replication of Novel Murine Astroviruses. *J. Virol.* **86**, 12262–12270 (2012).

49. Compton, S. R., Booth, C. J. & Macy, J. D. Murine Astrovirus Infection and Transmission in Neonatal CD1 Mice. *J. Am. Assoc. Lab. Anim. Sci.* **56**, (2017).

50. Sebire, N. J. Pathology of astrovirus associated diarrhoea in a paediatric bone marrow transplant recipient. *J. Clin. Pathol.* **57**, 1001–1003 (2004).

51. Cortez, V. *et al.* Characterizing a Murine Model for Astrovirus Using Viral Isolates from Persistently Infected Immunocompromised Mice. *J. Virol.* **93**, e00223-19 (2019).

52. Cortez, V. *et al.* Astrovirus infects actively secreting goblet cells and alters the gut mucus barrier. *Nat. Commun.* **11**, 2097 (2020).

53. Ingle, H. *et al.* Murine astrovirus tropism for goblet cells and enterocytes facilitates an IFN-λ response in vivo and in enteroid cultures. *Mucosal Immunol.* **14**, 751–761 (2021).

54. Triana, S. *et al.* Single-cell transcriptomics reveals immune response of intestinal cell types to viral infection. *Mol. Syst. Biol.* **17**, e9833 (2021).

55. Kolawole, A. O. *et al.* Astrovirus replication in human intestinal enteroids reveals multi-cellular tropism and an intricate host innate immune landscape. *PLOS Pathog.* **15**, e1008057 (2019).

56. Sanchez-Fauquier, A. *et al.* Characterization of a Human Astrovirus Serotype 2 Structural Protein (VP26) That Contains an Epitope Involved in Virus Neutralization. *Virology* **201**, 312–320 (1994).

57. Zheng, H. *et al. CheckMyMetal*: a macromolecular metal-binding validation tool. *Acta Crystallogr. Sect. Struct. Biol.* **73**, 223–233 (2017).

58. Zimmermann, L. *et al.* A Completely Reimplemented MPI Bioinformatics Toolkit with a New HHpred Server at its Core. *J. Mol. Biol.* **430**, 2237–2243 (2018).

59. Emsley, P., Lohkamp, B., Scott, W. G. & Cowtan, K. Features and development of *Coot*. *Acta Crystallogr. D Biol. Crystallogr.* **66**, 486–501 (2010).

60. Liebschner, D. *et al.* Macromolecular structure determination using X-rays, neutrons and electrons: recent developments in *Phenix*. *Acta Crystallogr. Sect. Struct. Biol.* **75**, 861–877 (2019).

61. Edgar, R. C. MUSCLE: multiple sequence alignment with high accuracy and high throughput. *Nucleic Acids Res.* **32**, 1792–1797 (2004).

62. Jones, D. T., Taylor, W. R. & Thornton, J. M. The rapid generation of mutation data matrices from protein sequences. *Bioinformatics* **8**, 275–282 (1992).

63. Kumar, S., Stecher, G., Li, M., Knyaz, C. & Tamura, K. MEGA X: Molecular Evolutionary Genetics Analysis across Computing Platforms. *Mol. Biol. Evol.* **35**, 1547–1549 (2018).

64. Zhang, Y. TM-align: a protein structure alignment algorithm based on the TM-score. *Nucleic Acids Res.* **33**, 2302–2309 (2005).

65. Delgado-Cunningham, K., López, T., Khatib, F., Arias, C. F. & DuBois, R. M. Structure of the divergent human astrovirus MLB capsid spike. *Structure* **30**, 1573-1581.e3 (2022).

66. Schmidt, K. *et al.* Development of a multiplex serological assay reveals a worldwide distribution of murine astrovirus infections in laboratory mice. *PLOS ONE* **12**, e0187174 (2017).

67. Kawagishi, T. *et al.* Mucosal and systemic neutralizing antibodies to norovirus induced in infant mice orally inoculated with recombinant rotaviruses. *Proc. Natl. Acad. Sci.* **120**, e2214421120 (2023).

68. Schindelin, J. *et al.* Fiji: an open-source platform for biological-image analysis. *Nat. Methods* **9**, 676–682 (2012).